J. Fluid Mech. (2019), *vol.* 862, *pp.* 816–844.
doi:10.1017/jfm.2018.958

Absolute and convective instabilities in electrohydrodynamic flow subjected to a Poiseuille flow: a linear analysis

Fang Li[1], Bo-Fu Wang[2], Zhen-Hua Wan[1], Jian Wu[3] and Mengqi Zhang[4,†]

[1]Department of Modern Mechanics, University of Science and Technology of China, Anhui 230027, PR China

[2]Shanghai Institute of Applied Mathematics and Mechanics, and Shanghai Key Laboratory of Mechanics in Energy Engineering, Shanghai University, Shanghai 200072, PR China

[3]School of Energy Science and Engineering, Harbin Institute of Technology, Harbin 150001, PR China

[4]Department of Mechanical Engineering, National University of Singapore, 9 Engineering Drive 1, 117575 Singapore

(Received 25 April 2018; revised 14 November 2018; accepted 27 November 2018; first published online 16 January 2019)

We present a study of absolute and convective instabilities in electrohydrodynamic flow subjected to a Poiseuille flow (EHD-Poiseuille). The electric field is imposed on two infinite flat plates filled with a non-conducting dielectric fluid with unipolar ion injection. Mathematically, the dispersion relation of the linearised problem is studied based on the asymptotic response of an impulse disturbance imposed on the base EHD-Poiseuille flow. Transverse, longitudinal and oblique rolls are investigated to identify the saddle point satisfying the pinching condition in the corresponding complex wavenumber space. It is found that when the ratio of Coulomb force to viscous force increases, the transverse rolls can transit from convective instability to absolute instability. The ratio of hydrodynamic mobility to electric mobility, which exerts negligible effect on the linear stability criterion when the cross-flow is small, has significant influence on the convective–absolute instability transition, especially when the ratio is small. As we change the value of the mobility ratio, a saddle point shift phenomenon occurs in the case of transverse rolls. The unstable longitudinal rolls are convectively unstable as long as there is a cross-flow, a result which is deduced from a one-mode Galerkin approximation. Longitudinal rolls have a larger growth rate than transverse rolls except for a small cross-flow. Finally, regarding the oblique rolls, a numerical search for the saddle point simultaneously in the complex streamwise and transverse wavenumber spaces always yields an absolute transverse wavenumber of zero, implying that oblique rolls give way to transverse rolls when the flow is unstable.

Key words: absolute/convective instability, MHD and electrohydrodynamics

† Email address for correspondence: mpezmq@nus.edu.sg

1. Introduction

1.1. *Electrohydrodynamic flow*

Studies on electrohydrodynamic flow (EHD) are concerned with the dual effects of electrostatics and hydrodynamics, which are governed respectively by Maxwell's equations in the quasi-electrostatic limit and the Navier–Stokes equations, cf. Castellanos (1998), Kikuchi (2001). There are mainly two ion creation mechanisms in EHD, one being ion injection and the other being dissociation of chemical species (in this paper, we focus on the first mechanism). EHD flow is not only of theoretical interest with research topics including flow stability and turbulence (Castellanos 1998) and dusty plasma and lightning modelling (Kikuchi 2001), but also has significant industrial/commercial applications, such as EHD pumps (Stuetzer 1960; Melcher & Firebaugh 1967; Darabi *et al.* 2002), micro-/nano-scale drug delivery (Chakraborty *et al.* 2009), EHD heat enhancement (Allen & Karayiannis 1995), electrostatic precipitators (White 1965) and charge injection atomisers (Shrimpton 2009).

Theoretically, the flow dynamics in EHD is complex and far from being fully understood. Studying EHD flow can contribute to our current knowledge of complex system. The experimental work by Malraison & Atten (1982) studied the turbulent EHD flow subject to unipolar ion injection (such a flow is called electroconvection). The authors observed that an exponential decay of the power spectral density was found when the viscous force is dominant but a power-law decay was observed when the inertial force is dominant. By high-pass filtering the intensity fluctuation of the turbulent signal, they demonstrated that the exponential decay is related to the burst of intermittency in the flow, consistent with the theoretical study by Frisch & Morf (1981). Electroconvection has been often compared to the well-studied turbulent natural convection. It has been demonstrated that in Rayleigh–Bénard convection (RBC), the dimension of the corresponding strange attractor is approximately of order 3 (experimental work by Dubois (1982) indicated a value of 2.8), while Atten *et al.* (1984) showed that the turbulent EHD flow corresponds to a strange attractor of very large or infinite order (Castellanos 1991). The flow instability mechanism is also different in electroconvection and natural convection. It is well known that the bifurcation mechanism in RBC under the Boussinesq approximation is of a supercritical nature (Cross 1980), whereas electroconvection takes a subcritical route (Atten & Lacroix 1979; Zhang 2016). This is partially because, in RBC, molecular diffusion constitutes the principal dissipative mechanism, whereas in EHD flow, it is the ion drift velocity that diffuses perturbations in the fluid with a hysteresis loop (Atten & Lacroix 1974). Thus, there are many unique features of EHD flow that await exploration in view of a dynamical system approach. As another example, the interaction between longitudinal convection rolls and transverse waves in RBC-Poiseuille flow under the Boussinesq approximation has long been studied in terms of a supercritical–subcritical bifurcation (Fujimura & Kelly 1995). Subcritical–subcritical interaction therefore cannot be discussed in this flow setting. EHD-Poiseuille flow serves to provide one example of this type of interaction.

Studying the combined EHD-Poiseuille flow also bears practical purposes. In a broad sense, we can investigate the interaction between EHD and shear and viscous effects in this configuration. The electroviscous (EV) phenomenon, which refers to the increase of apparent viscosity in bulk flow as a result of the electrostatic effect, has been investigated in EHD-Poiseuille flow (Atten & Honda 1982) in order to decrease the amplitude of undesirable vibration. The EV damper is more favourable than other passive devices or active methods in cost, weight and size. Besides, EHD-Poiseuille

flow (with corona discharge as the ion generation mechanism) can also be related to the electrostatic precipitator or ESP (McCluskey & Atten 1984; Atten, McCluskey & Lahjomri 1987), which is widely used in reducing industrial particulate emissions (White 1965) and also recently finds applications in sampling for bioaerosols (Pardon *et al.* 2015). The turbulence in ESP will influence the behaviour of charged particles in the flow and is crucial to optimise precipitator efficiency. Finally, EHD can also be studied in the light of turbulent flow control to investigate how the wall-bounded shear flow can be manipulated by the electric field. It can be envisioned that the electric field, by forming counter-rotating streamwise vortices, is able to reduce the skin drag because the vortex can modify the turbulent structures in the near-wall region (Schoppa & Hussain 1998). In a related context, the roll structures that appear in EHD-Couette flow have been investigated by Kourmatzis & Shrimpton (2016) to study the EHD in a shear flow, which has applications in electrostatic atomisation and heat transfer enhancement.

In the following, we first review the relevant research works on EHD-Poiseuille flow (mostly linear stability analyses), then discuss the concept of absolute and convective instabilities and finally introduce the aim and structure of this paper.

Atten & Honda (1982) first conducted an experimental study on the EHD-Poiseuille flow focusing on the EV effect. They found that the pressure drop in the flow subject to an electric field can be 20 times higher than that without an electric field. They attributed the increase to the electrically induced secondary motion. This implies that the electric field can indeed dramatically change the flow characteristics of a cross-flow. Castellanos & Agrait (1992) investigated the linear stability of EHD flow in plane Poiseuille flow or Couette flow. They conducted an energy analysis of the disturbances to explain the instability that arises from the electric or inertial effect. It was found that EHD-Poiseuille flow is stabilised when the Reynolds number (Re) is less than a certain value but destabilised at higher Re (Reynolds number measures the amplitude of the Poiseuille flow). The transverse rolls are stabilised when the ratio of hydrodynamic mobility to ion mobility M increases (see § 2.2 below for its mathematical definition). Lara, Castellanos & Pontiga (1997) found that when M is large, the charge field tends to be more fluctuating. Similar to Castellanos & Agrait (1992), with increasing M, they also noticed the flow stability in the range of $0 < Re < 100$. By analysing the hydrodynamic energy of a perturbation caused by an electric force via a method of stationary phase, the authors demonstrated that, at the neutral curve, the critical stability parameter T (which measures the relative importance of Coulomb force to viscous force) is proportional to M, consistent with their numerical results. Recently, Zhang *et al.* (2015) studied the linear stability analysis of EHD flow with and without Poiseuille flow. This work performed a non-modal linear stability analysis (which calculates the transient growth of disturbance energy, see Schmid 2007). In the part relating to EHD-Poiseuille flow, it was confirmed that Poiseuille flow is destabilised by the electric field. The transient growth in EHD-Poiseuille flow also becomes significantly large with increasing strength of the electric field, implying that the electric field destabilises the Poiseuille flow in a short time. Besides the linear stability analyses, there were also works on nonlinear stability analyses (weakly nonlinear and energy analyses) of EHD-Poiseuille flow, which are less relevant to this work. The interested readers are referred to Félici (1971), Atten & Lacroix (1979), Richardson & Deo (1986), Zhang (2016).

1.2. *Absolute and convective instabilities*

The concept of absolute and convective instabilities is important in categorising convective flow systems (Briggs 1964; Huerre & Monkewitz 1990; Chomaz 2005). It is a general framework to address the linear instability development of a disturbance in both space and time or wavelength and frequency. When an infinitesimal impulse is imposed on a base flow, the flow system will undergo one of the three different routes, i.e. being stable, convectively unstable or absolutely unstable. If the disturbance decays with time at all spatial positions, the flow eventually returns to its undisturbed state and the corresponding base flow is regarded as stable. The flow is referred to as convectively unstable if the impulse disturbance grows within at least one moving frame of reference, but decays locally where it is initially excited. In other words, the disturbance is amplified along the spatial coordinate, a situation which necessitates a spatial linear stability analysis. This type of flow, often referred to as a noise amplifier, is extremely sensitive to externally imposed disturbance/forcing, and therefore will be very hard to control/manipulate in a real situation. Finally, if the disturbance grows with time at all spatial positions, the flow is then absolutely unstable. Accordingly, a temporal linear stability analysis is more suitable in this case. Absolutely unstable flow is often characterised by an inherent instability mechanism and is less dependent on the external disturbance/forcing. In such flows, there is usually a specific spatial region which acts as a 'wavemaker' associated with a preferred frequency. These flows are conventionally called an oscillator.

The absolute and convective instabilities were first systematically studied by plasma physicists (Briggs 1964; Bers 1983). In the field of hydrodynamic stability, extensive studies have also been conducted. Gage & Reid (1968) examined the long-time behaviour of the Green function in a thermally stratified plane Poiseuille flow. In a series of papers by Gaster (1965, 1968, 1975, 1981), the disturbance growth in both space and time was investigated. A very well received work in this field is due to Huerre & Monkewitz (1985), who studied, by means of a steepest descent method (Whitham 1974), the absolute and convective instabilities in free shear layers formulated as a problem of estimating the asymptotic response of an impulse excited on the base flow. They found that if the mixing layer is convectively unstable (the velocity ratio in the free shear layer is smaller than a critical value $R_t = 1.315$), the flow can only be marked by spatially growing waves, whereas, when the velocity ratio is larger than R_t, the instability wave will develop temporally (absolutely unstable). Later, the convective nature of Poiseuille flow was demonstrated by Deissler (1987). When a convectively unstable system is superposed on an absolutely unstable system, an interesting question arises as to where the border between absolute and convective instabilities lies in the new system. This problem is important because, depending on its convective (noise amplifier) or absolute (oscillator) nature, the unstable flow will behave fundamentally differently and it will have a significant influence on deciding the flow control strategy, as we have elaborated above.

This kind of study was exemplified by the superposed system of Poiseuille flow and Rayleigh–Bénard convection under the Boussinesq assumption (Gage & Reid 1968; Müller, Lücke & Kamps 1992; Müller, Tveitereid & Trainoff 1993; Kelly 1994; Tveitereid & Müller 1994; Carrière & Monkewitz 1999; Carrière, Monkewitz & Martinand 2004; Grandjean & Monkewitz 2009). Rayleigh–Bénard convection (RBC) is driven by a thermal gradient field across two infinite flat plates. The buoyancy force drives the fluid to form convective motion. As a linear RBC can only support stationary waves, the system is absolutely unstable whenever it is unstable. Once RBC is superposed on a Poiseuille flow (RBP), the new system's absolute/convective

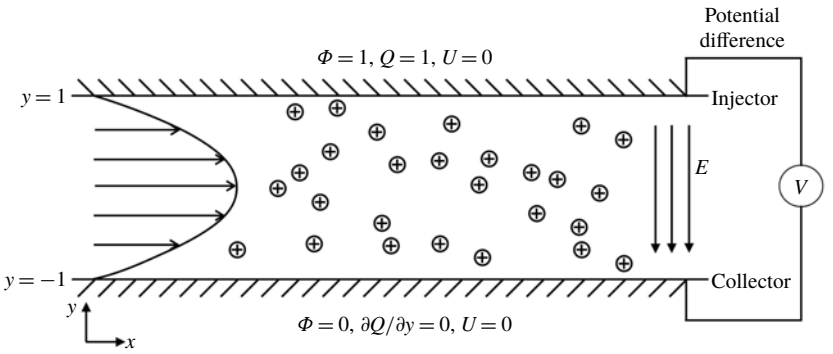

FIGURE 1. A two-dimensional schematic representation of EHD-Poiseuille flow.

instability border has to be pinned down in the parameter space spanned by the Reynolds number Re (ratio of inertia to viscosity), Rayleigh number Ra (ratio of buoyancy force to viscosity force) and Prandtl number Pr (ratio of viscous diffusion to thermal diffusion). Carrière & Monkewitz (1999) addressed this problem with the dispersion relation derived from the linearised Navier–Stokes equation and they found that the convective–absolute transition in RBP always corresponds to transverse rolls when the Rayleigh number exceeds a critical value. On the other hand, the system remains convectively unstable with respect to longitudinal rolls for all non-zero Re.

1.3. *Current work*

We consider here a specific EHD configuration with unipolar injection in Poiseuille flow (see figure 1) where the ions are injected from one of two infinite flat plates filled with a non-conducting dielectric fluid and forced to move to the other plate under the action of Coulomb force as a result of the imposed electric field. As EHD shares commonalities with RBC, it also raises the question, similarly to RBP, regarding where the border between the absolute and convective instabilities is once the EHD is subjected to a cross-flow. Nevertheless, the absolute and convective instabilities in EHD-Poiseuille flow have not been investigated so far. This piece of information can be beneficial, e.g. in understanding the flow behaviour in ESP, thus improving its particle collection efficiency. Because of the aforementioned scientific significance and practical applications of EHD-Poiseuille flow, we are prompted to conduct such a study to better understand it. We will analyse the dispersion relation of linearised EHD-Poiseuille flow via a spatio-temporal linear stability analysis, a theory which is based on the long-term asymptotic response of an impulse imposed on the base flow. A careful search of the literature indicates that there is no experimental work designed specifically for investigating the absolute and convective instabilities in EHD-Poiseuille flow. Therefore, our theoretical results to be presented below may serve as a source for comparison of future experimental works relevant to this specific problem.

Finally, we mention in passing that in a broader context of electrohydrodynamic and electrokinetic flow, the absolute and convective instabilities of electrokinetic flow with conductivity gradients have been studied by Chen *et al.* (2005). Their EHD flow is different from what we consider here; the ion generation mechanism in their case is due to the conductivity gradients based on the leaky dielectric model (Saville 1997).

The paper is organised as follows. In § 2, we present the theoretical model of the electric field and hydrodynamic field and derive the linearised governing

equations. The theoretical tool for studying absolute and convective instabilities is then formulated following Huerre & Monkewitz (1985), Carrière & Monkewitz (1999). In § 3, we delimit the convective/absolute instabilities border that is affected by various non-dimensional parameters for transverse, longitudinal and oblique rolls and provide physical interpretations of our findings. Finally, in § 4, we conclude the paper by summarising the results.

2. Theoretical model and equations

2.1. *Theoretical modelling*

We consider the flow of an incompressible Newtonian viscous dielectric liquid between two infinite planes, see figure 1. The Cartesian coordinate system (x, y, z) is used to describe the problem, with x, y and z being streamwise, wall-normal and transverse coordinates, respectively. The flow is maintained by a constant pressure gradient in x direction. A direct-current (DC) electric voltage V_0 is imposed across the two plates. Meanwhile, charges of density Q_0 are injected into the liquid from the upper plane (injector). The flow is affected by the electric Coulomb force acting on the charged ions. The Navier–Stokes equations in this scenario read (the superscript * indicates a dimensional variable)

$$\boldsymbol{\nabla}^* \cdot \boldsymbol{u}^* = 0, \tag{2.1}$$

$$\rho \frac{\partial \boldsymbol{u}^*}{\partial t^*} + \rho(\boldsymbol{u}^* \cdot \boldsymbol{\nabla}^*)\boldsymbol{u}^* = -\boldsymbol{\nabla}^* p^* + \mu \nabla^{*2} \boldsymbol{u}^* + q^* \boldsymbol{E}^*, \tag{2.2}$$

where $\boldsymbol{u}^*$ is the velocity of the liquid (with streamwise velocity u^*, wall-normal velocity v^* and transverse velocity w^*), ρ is the density of the liquid, p^* is the pressure and μ is the dynamic viscosity of the liquid (assuming that the system is isothermal and homogeneous). The last term in (2.2), $q^*\boldsymbol{E}^*$, is the Coulomb force. Since we consider a DC voltage and a constant electric permittivity, it is legitimate to consider only the Coulomb force term, following Castellanos (1998), Kikuchi (2001) or our previous work Zhang *et al.* (2015).

The dynamics of injected charged ions complies with Maxwell's equations. We consider dielectric liquids of low conductivity. These fluids can exhibit nonlinear current–voltage characteristics (Atten & Honda 1982). The magnetic field and Joule heating effect are neglected. The governing equations for the electric field are Maxwell's equations in the quasi-electrostatic limit (Castellanos 1998; Kikuchi 2001), i.e.

$$\boldsymbol{\nabla}^* \times \boldsymbol{E}^* = 0, \tag{2.3}$$

$$\boldsymbol{\nabla}^* \cdot \boldsymbol{D}^* = q^*, \tag{2.4}$$

$$\frac{\partial q^*}{\partial t^*} + \boldsymbol{\nabla}^* \cdot \boldsymbol{j}^* = 0 \quad \text{with } \boldsymbol{j}^* = K\boldsymbol{E}^* q^* + \boldsymbol{u}^* q^* - D_v \boldsymbol{\nabla}^* q^*, \tag{2.5}$$

where $\boldsymbol{E}^*$ is the electric field intensity, $\boldsymbol{D}^* = \epsilon \boldsymbol{E}^*$ the electric displacement vector with ϵ being the electric permittivity of the liquid, q^* the volume charge density, $\boldsymbol{j}^*$ the electric current density, K the ionic mobility, D_v the charge diffusion coefficient. Since the electric field is irrotational (2.3), it is appropriate to introduce an electric potential function ϕ^*, so that $\boldsymbol{E}^* = -\boldsymbol{\nabla}^* \phi^*$. From (2.4),

$$\nabla^{*2} \phi^* = -\frac{q^*}{\epsilon}. \tag{2.6}$$

At the upper plane (injector) $y^* = L$ and the lower plane (collector) $y^* = -L$, where L is the half-distance between the two planes, the following boundary conditions are imposed:

(i) no-slip and no-penetration conditions for the velocity field, i.e. $\boldsymbol{u}^*|_{y^*=\pm L}=0$;
(ii) Dirichlet conditions for the electric potential, i.e. $\phi^*|_{y^*=L}=V_0$ and $\phi^*|_{y^*=-L}=0$;
(iii) the charge density at the injector is constant and the y-direction gradient of the charge density at the collector is zero, i.e. $q^*|_{y^*=L}=Q_0$ and $\partial q^*/\partial y^*|_{y^*=-L}=0$, see Pérez & Castellanos (1989).

2.2. *Non-dimensionalisation*

Choosing L, KV_0/L (ion drift velocity), $\rho K^2V_0^2/L^2$, V_0, V_0/L and Q_0 as the characteristic length, velocity, pressure, electric potential, electric field and charge density, respectively, the equations governing the system are non-dimensionalised as follows

$$\boldsymbol{\nabla}\cdot\boldsymbol{u}=0, \tag{2.7}$$

$$\frac{\partial \boldsymbol{u}}{\partial t}+(\boldsymbol{u}\cdot\boldsymbol{\nabla})\boldsymbol{u}=-\boldsymbol{\nabla}p+\frac{M^2}{T}\nabla^2\boldsymbol{u}+CM^2q\boldsymbol{E}, \tag{2.8}$$

$$\boldsymbol{E}=-\boldsymbol{\nabla}\phi, \tag{2.9}$$

$$\nabla^2\phi=-Cq, \tag{2.10}$$

$$\frac{\partial q}{\partial t}+\boldsymbol{\nabla}\cdot[q(\boldsymbol{E}+\boldsymbol{u})]=\frac{1}{Fe}\nabla^2q, \tag{2.11}$$

where the symbols without superscript * denote the corresponding dimensionless variables. There are four dimensionless parameters appearing in the governing equations:

(i) $T=\epsilon V_0/K\mu$: the Taylor number measuring the relative importance of the Coulomb force to the viscous force for a constant ion injection level;
(ii) $C=Q_0L^2/\epsilon V_0$: the level of ion injection;
(iii) $M=\sqrt{\epsilon/\rho}/K$: the ratio between hydrodynamic mobility and electrical mobility of ions in the electric field (the drift velocity is $K\boldsymbol{E}$);
(iv) $Fe=KV_0/D_v$: the ratio of ion drift to charge diffusion in electric current.

The dimensionless boundary conditions are $\boldsymbol{u}|_{y=\pm1}=0$, $\phi|_{y=1}=1$, $\phi|_{y=-1}=0$, $q|_{y=1}=1$ and $\partial q/\partial y|_{y=-1}=0$. There are certainly other possibilities for non-dimensionalisation; for example, Lara *et al.* (1997) use the time and velocity scales of particle diffusion to characterise their equations.

The base flow is sustained by a constant pressure gradient $-\mathrm{d}P/\mathrm{d}x$ along the streamwise direction. From the time-independent solution of the momentum equation (2.8), which is subject to the no-slip boundary conditions, we have

$$U(y)=-\frac{1}{2}\frac{\mathrm{d}P}{\mathrm{d}x}\frac{T}{M^2}(1-y^2)=-\frac{1}{2}\frac{\mathrm{d}P}{\mathrm{d}x}Re\Gamma(1-y^2), \tag{2.12}$$

where $Re=U_0L/\nu$ is the Reynolds number accounting for the ratio between inertia and viscosity (U_0 is the characteristic velocity scale in the flow). The first equation in (2.12) implies that solely modifying the strength of the electric field (i.e. changing T) could change the base flow. This is inherently related to the way we non-dimensionalise the system. It is more instructive to look at the second equation, which makes Re explicit. There also appears a non-dimensional number $\Gamma=(T/M^2)(1/Re)=KV_0/U_0L$ linking the ion drift to ion advection (in the absence of a proper name, we call it Γ), which has been discussed in Zhang *et al.* (2015).

In most of the experiments involving a cross-flow, the common way of changing the base flow is to modify the pressure gradient; whereas in micro-/nano-scale systems, it is difficult to achieve this. The second expression indicates that one can modify the ratio of ion drift to ion advection in order to realise the same goal. In this work, we will change collectively the value of $-(1/2)(\mathrm{d}P/\mathrm{d}x)Re\Gamma$ to see the influence of the magnitude of the base cross-flow on the convective/absolute instability in EHD-Poiseuille flow. For the ease of discussion, we will hereafter call this combined non-dimensional number $\mathcal{U}$, so the base flow becomes $U(y)=\mathcal{U}(1-y^2)$.

The dimensionless differential equation for the base electric potential $\Phi(y)$ is

$$(D^2\Phi)^2+D\Phi D^3\Phi+\frac{1}{Fe}D^4\Phi=0, \tag{2.13}$$

with the boundary conditions $\Phi|_{y=1}=1$, $\Phi|_{y=-1}=0$, $D^2\Phi|_{y=1}=-C$ and $D^3\Phi|_{y=-1}=0$. It is difficult to solve (2.13) analytically subject to these boundary conditions; therefore, we use a numerical solver to obtain the base state of Φ^* following Zhang *et al.* (2015), Zhang (2016).

2.3. *Linearisation*

In the linear stability analysis, the physical quantities are decomposed into a basic part and a perturbation part, i.e. $\boldsymbol{u}=\boldsymbol{U}+\boldsymbol{u}'$, $p=P+p'$, $\boldsymbol{E}=\boldsymbol{E}_0+\boldsymbol{E}'$, $q=Q+q'$ and $\phi=\Phi+\phi'$, where the prime $'$ denotes the perturbation parts. Substitution of the decompositions into the governing equations and boundary conditions yields the following linearised equations

$$\nabla\cdot\boldsymbol{u}'=0, \tag{2.14}$$

$$\frac{\partial\boldsymbol{u}'}{\partial t}+(\boldsymbol{U}\cdot\nabla)\boldsymbol{u}'+(\boldsymbol{u}'\cdot\nabla)\boldsymbol{U}=-\nabla p'+\frac{M^2}{T}\nabla^2\boldsymbol{u}'+CM^2(Q\boldsymbol{E}'+\boldsymbol{E}_0q'), \tag{2.15}$$

$$\boldsymbol{E}'=-\nabla\phi', \tag{2.16}$$

$$\nabla^2\phi'=-Cq', \tag{2.17}$$

$$\frac{\partial q'}{\partial t}+\nabla\cdot[Q(\boldsymbol{E}'+\boldsymbol{u}')+q'(\boldsymbol{E}_0+\boldsymbol{U})]=\frac{1}{Fe}\nabla^2q', \tag{2.18}$$

with $\boldsymbol{u}'|_{y=\pm1}=0$, $\phi'|_{y=\pm1}=0$, $q'|_{y=1}=0$ and $\partial q'/\partial y|_{y=-1}=0$. Hereinafter, the primes on the perturbation quantities are dropped for the sake of brevity. It should be mentioned that in the case of space-charge limit (SCL, that is infinite C) and no charge diffusion (infinite Fe), Atten & Moreau (1972), Lara *et al.* (1997) argued that the boundary condition $q'|_{y=1}=0$ should be modified to be consistent with the equations. As we consider finite values of C and Fe, there is no need to change the above boundary conditions.

For the electric field, it is possible to re-write (2.16)–(2.18) into one equation in terms of the electric potential perturbation ϕ. The linearised governing equations can then be re-cast in terms of the wall-normal vorticity $\eta=\partial u/\partial z-\partial w/\partial x$, wall-normal velocity v and electric potential ϕ. Since Squire's theorem is valid in EHD-Poiseuille flow (Zhang *et al.* 2015), it is legitimate and sufficient to consider only a v–ϕ formulation for our purpose

$$\begin{aligned}\frac{\partial\nabla^2v}{\partial t}=&\left(-U\frac{\partial}{\partial x}\nabla^2+D^2U\frac{\partial}{\partial x}+\frac{M^2}{T}\nabla^4\right)v\\&+M^2\left[-D^3\Phi\left(\nabla^2-\frac{\partial^2}{\partial y^2}\right)\phi+D\Phi\left(\nabla^2-\frac{\partial^2}{\partial y^2}\right)\nabla^2\phi\right],\end{aligned} \tag{2.19}$$

$$\frac{\partial \nabla^2 \phi}{\partial t} = D^3\Phi \frac{\partial \phi}{\partial y} + 2D^2\Phi \nabla^2 \phi + D\Phi \frac{\partial \nabla^2 \phi}{\partial y} - U\frac{\partial \nabla^2 \phi}{\partial x} - D^3\Phi v + \frac{1}{Fe}\nabla^4 \phi, \tag{2.20}$$

with the boundary conditions

$$v(y=\pm 1)=0, \quad \frac{\partial v}{\partial y}(y=\pm 1)=0, \tag{2.21a,b}$$

$$\phi(y=\pm 1)=0, \quad \frac{\partial^2 \phi}{\partial y^2}(y=1)=0, \quad \frac{\partial^3 \phi}{\partial y^3}(y=-1)=0. \tag{2.21c–e}$$

2.4. *Absolute and convective instability analysis*

Suppose that a localised impulse perturbation is imposed on the base flow. In order to determine the absolute and convective instability of the flow, we can study the spatio-temporal response of the impulse disturbance. The following theoretical development is due to Huerre & Monkewitz (1985), Carrière & Monkewitz (1999). The linearised system (2.19)–(2.20) can be written in a matrix form

$$\mathscr{A}\frac{\partial \boldsymbol{h}}{\partial t} + \mathscr{B}\boldsymbol{h} = 0, \tag{2.22}$$

where

$$\boldsymbol{h} = (v, \phi)^{\mathrm{T}}, \quad \mathscr{A} = \begin{bmatrix} \nabla^2 & 0 \\ 0 & \nabla^2 \end{bmatrix}, \quad \mathscr{B} = \begin{bmatrix} \mathscr{L}_{os} & \mathscr{L}_{v\phi} \\ \mathscr{L}_{\phi v} & \mathscr{L}_{\phi\phi} \end{bmatrix}, \tag{2.23a–c}$$

the superscript T denotes transpose, and the expressions of $\mathscr{L}_{os}$, $\mathscr{L}_{v\phi}$, $\mathscr{L}_{\phi v}$ and $\mathscr{L}_{\phi\phi}$ can be easily obtained from (2.19)–(2.20). Imposing an impulse in (2.22), we get

$$\mathscr{A}\frac{\partial \boldsymbol{G}}{\partial t} + \mathscr{B}\boldsymbol{G} = \boldsymbol{F}, \tag{2.24}$$

where $\boldsymbol{F}$ is the impulse of the form

$$\boldsymbol{F} = (F_v, F_\phi)^{\mathrm{T}} = (a_v(y), a_\phi(y))^{\mathrm{T}}\delta(x)\delta(z)\delta(t), \tag{2.25}$$

a_v, a_ϕ are the shape functions, and δ is the Kronecker delta function.

To determine the absolute/convective instability of the flow, one can check the long-time behaviour of Green's function $\boldsymbol{G}$ by using the method of steepest descent (Whitham 1974) twice in the complex α- and complex β-plane. After some standard manipulations of the equations following Huerre & Monkewitz (1985), Carrière & Monkewitz (1999), the expression for Green's function at long times is

$$\begin{aligned} \boldsymbol{G}(x, y, z, t) \;=\; & \frac{-\mathrm{i}}{2\pi t}\sum_n \left[\frac{\partial^2 \omega_n}{\partial \alpha^2}(\alpha_{sn}, \beta_{sn})\frac{\partial^2 \omega_n}{\partial \beta^2}(\alpha_{sn}, \beta_{sn}) - \left(\frac{\partial^2 \omega_n}{\partial \alpha \partial \beta}\right)^2(\alpha_{sn}, \beta_{sn})\right]^{-1/2} \\ & \times \langle \hat{\hat{\boldsymbol{h}}}_n^{\dagger}(\alpha_{sn}, y, \beta_{sn}), \hat{\hat{\boldsymbol{F}}}(y)\rangle \hat{\hat{\boldsymbol{h}}}_n(\alpha_{sn}, y, \beta_{sn}) \exp(\mathrm{i}(\alpha_{sn}x + \beta_{sn}z - \omega_{sn}t)), \end{aligned} \tag{2.26}$$

where the subscript s denotes the saddle points, and α_{sn}, β_{sn} and $\omega_{sn}(\alpha_{sn}, \beta_{sn})$ are the complex streamwise wavenumber, transverse wavenumber and frequency at the saddle point determined by

$$\frac{\partial \omega_n}{\partial \alpha}(\alpha_{sn}, \beta_{sn}) = \frac{x}{t}, \quad \frac{\partial \omega_n}{\partial \beta}(\alpha_{sn}, \beta_{sn}) = \frac{z}{t}. \tag{2.27a,b}$$

The equation (2.27) implies that the group velocity at a saddle point is real.

On the other hand, from (2.26), the amplitude of Green's function at long times is proportional to $\mathrm{e}^{\sigma_{i,max}t}/t$, where $\sigma_{i,max}$ is the maximum growth rate along the ray $x/t =$ const. and $z/t =$ const., i.e.

$$\sigma_{i,max} = \left[\omega_{sn,i}(\alpha_{sn}, \beta_{sn}) - \alpha_{sn,i}\frac{x}{t} - \beta_{sn,i}\frac{z}{t}\right]_{max}, \tag{2.28}$$

where the subscript i denotes the imaginary part. To get $\sigma_{i,max}$, one needs to solve $\partial\sigma_i/\partial(x/t) = 0$ and $\partial\sigma_i/\partial(z/t) = 0$, which results in $\alpha_{sn,i} = \beta_{sn,i} = 0$, implying that when the streamwise wavenumber α and the transverse wavenumber β are real valued, the growth rate σ_i is maximum. That is, the temporal mode is the most unstable/least stable. Therefore, to judge the stability of the flow, we look into the maximum temporal growth rate $\omega_{i,max} = \max\{\omega_i(\alpha, \beta)$, for $\forall$ real $\alpha, \beta\}$:

(i) if $\omega_{i,max} < 0$, the flow is linearly stable;
(ii) if $\omega_{i,max} = 0$, the flow is neutrally stable;
(iii) if $\omega_{i,max} > 0$, the flow is linearly unstable.

From (2.26), we can deduce that an unstable parallel flow is convectively unstable if $\lim_{t\to\infty} \boldsymbol{G}(x, y, z, t) = 0$ and is absolutely unstable if $\lim_{t\to\infty} \boldsymbol{G}(x, y, z, t) = \infty$. When $t \to \infty$, for any fixed location, $x/t \to 0$ and $z/t \to 0$, and (2.27) reduces to

$$\frac{\partial \omega_n}{\partial \alpha}(\alpha_{n0}, \beta_{n0}) = 0, \quad \frac{\partial \omega_n}{\partial \beta}(\alpha_{n0}, \beta_{n0}) = 0. \tag{2.29a,b}$$

Here α_{n0} and β_{n0} are the absolute wavenumbers, and $\omega_{n0}(\alpha_{n0}, \beta_{n0})$ the absolute frequency with its imaginary part $\omega_{n0,i}$ being the absolute growth rate. From (2.28), the maximum growth rate $\sigma_{i,max} = \max\{\omega_{n0,i}$, for all the saddle points$\}$. Apparently, if $\max\{\omega_{n0,i}\} > 0$, the flow is absolutely unstable; if $\max\{\omega_{n0,i}\} < 0$, the flow is convectively unstable. Therefore the study of absolute and convective instabilities of the flow becomes the study of its characteristics at saddle points by solving (2.29). The saddle point must satisfy the Briggs pinching criterion (Briggs 1964; Bers 1983). Another way of identifying the valid singular point is to search for the cusp point in the frequency space (Kupfer, Bers & Ram 1987).

3. Numerical results and discussions

3.1. *Numerical method*

The theoretical development in the above section dictates the finding of the saddle point/cusp point in the dispersion relation (2.24) in the wavenumber/frequency space. We deal with this task in a framework of spatio-temporal linear stability analysis, in which both wavenumber and frequency are complex. The way of locating the saddle point in both streamwise and transverse wavenumber spaces simultaneously is detailed in appendix A. The numerical problem is solved by using a Chebyshev

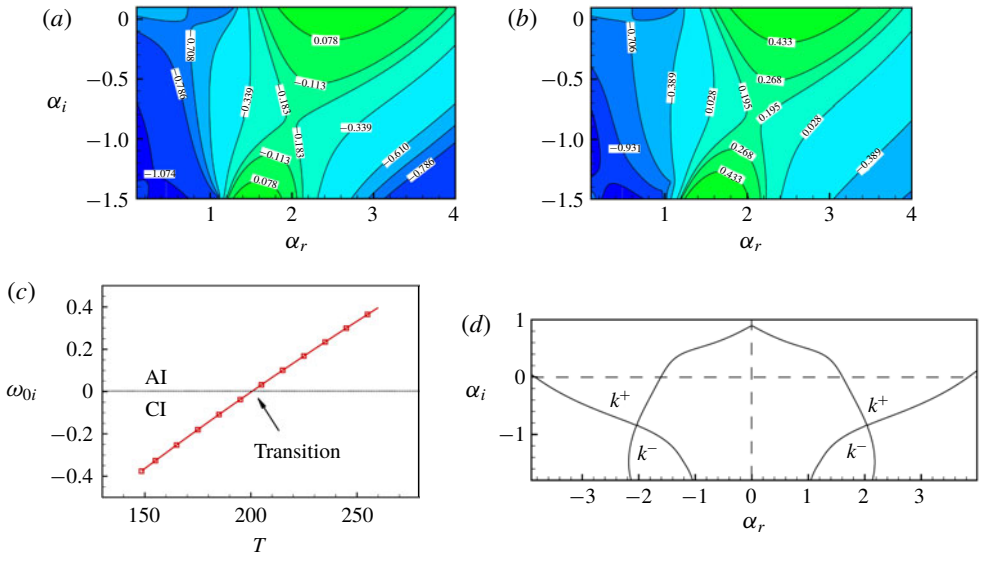

FIGURE 2. (Colour online) Typical ω_i-contours in the complex α-plane for transverse rolls for (*a*) $T = 175$ and (*b*) $T = 230$. (*c*) Absolute growth rate ω_{0i} versus Taylor's parameter T. AI represents absolute instability and CI convective instability. (*d*) The pinching condition when the absolute instability of transverse rolls is triggered at $T = 200.37$. k^+ denotes the spatial branch for which rolls propagate downstream while k^- denotes the spatial branch for which rolls propagate upstream. The parameters in this figure are $C = 50$, $M = 50$, $Fe = 10^4$.

spectral collocation method as in our previous works (Zhang *et al.* 2015; Zhang 2016) and hence the details are not repeated here. The new code has been verified by comparing the results against those in Zhang *et al.* (2015).

In the following we study the effects of various non-dimensional parameters on the absolute and convective instabilities of transverse, longitudinal and oblique rolls. For the ranges of the parameters, we consider those that can reflect the properties of the liquids in practice. M is from 3 to 100 (a range which can represent common dielectric fluids according to Lacroix, Atten & Hopfinger 1975), C is from 2.5 to 50 (approaching the SCL, which is the working condition for the charge injection atomiser where cross-flow is usually encountered, cf. Kourmatzis & Shrimpton 2014) and Fe is from 10^3 to 10^4 (see the discussion in Pérez & Castellanos 1989). We choose $\mathcal{U} = 1$ for most of the cases, except when we change it in figures 9, 10 and 14.

3.2. *Transverse rolls*

3.2.1. *Effect of T*

We first consider the transverse rolls (TR, $\beta = 0$). The electric field is found to influence significantly the absolute and convective instabilities of the system in this case. Typical contour plots of the imaginary part of the complex frequency, ω_i, in the complex α-plane are shown in figure 2(*a*,*b*) for two values of Taylor's parameter $T = 175, 230$ and the quantitative results are recorded in table 1. Apparently, there is one saddle point in each plot with $T = 175$ being convectively unstable and $T = 230$ absolutely unstable. The influence of T can be seen more clearly in figure 2(*c*), where

T	α_0	ω_0	Instability nature
175	1.993–0.853i	2.020–0.180i	Convective instability
200.37	2.039–0.841i	2.016+0i	Critical condition
230	2.082–0.823i	2.017+0.201i	Absolute instability

TABLE 1. The values of the parameters at the saddle points shown in figure 2 for transverse rolls. $T = 200.37$ is the critical condition where convective/absolute instability transitions.

the absolute growth rate ω_{0i} is increased as Taylor's parameter T increases. When T reaches some critical value (here $T \simeq 200.37$ at $C = 50$, $M = 50$, $Fe = 10^4$), the transition from convective to absolute instability occurs. The pinching condition has been examined for the saddle points, and an example is shown in figure 2(*d*).

The parameter T is related to the strength of the electric field. Experimentally, the most convenient way to modify the strength of the electric field is to change its electric potential V_0. Unfortunately, under the current scheme of non-dimensionalisation, V_0 appears in several non-dimensional parameters. In order to single out the effect of V_0 to compare with experimental works in the future, we use L/U_0 to scale the time, leading to the Reynolds number $Re = U_0 L/\nu$, a dimensionless number related to the electric voltage $Eu_1 = \varepsilon V_0^2/\rho U_0^2 L^2$, a dimensionless number related to the charge density $Eu_2 = Q_0^2 L^2/\varepsilon\rho U_0^2$, the same mobility ratio $M = \sqrt{\varepsilon/\rho}/K$ and the ratio between charge diffusion and ion convection $Du = D_v/U_0 L$. In such non-dimensionalisation, the voltage appears only in Eu_1. Note that the absolute growth rate under this new definition is different from the previous scaling. So here we use σ_{0i} in this part to distinguish it from the non-dimensional absolute growth rate ω_{0i}. The effect of Eu_1 on the absolute growth rate is shown in figure 3. We can see that the absolute growth rate σ_{0i} increases monotonically and almost linearly with the increase of Eu_1 near the transitional $Eu_1 = 2506.53$. This trend reflects the fact that the absolute growth rate is proportional to the squared electric voltage V_0^2, a fact which can be easily examined by experimentalists in the future.

3.2.2. *Effect of C*

The influence of the ion injection level C on the absolute growth rate ω_{0i} is shown in figure 4(*a*). We can observe that, as C increases, the line moves to the left, indicating that the transition from convective to absolute instability occurs at a smaller T for a larger injection level. However, the influence of the injection level is basically negligible at large C values close to SCL. Figure 4(*b*) shows the stability borders in the C–T plane, where the symbols (squares and triangles) represent the actually calculated data points, and the lines are the fitted results. At small C, the boundaries bend toward large T, while at large C, the boundaries approach some asymptotic values of T.

3.2.3. *Effect of M*

The influence of the mobility ratio M is more interesting and is shown in figure 5. In (*a*,*b*) for $M = 7$, two saddle points, labelled 'A' and 'B' in the figure, both satisfying the Briggs pinching criterion, are identified in the complex α-plane. At $T = 1495$ in (*a*), the saddle point A is dominant over the saddle point B with a larger ω_{0i} (at A, $\alpha_0 = 1.006 - 1.516\text{i}$, $\omega_0 = 1.633 + 0.0413\text{i}$; at B, $\alpha_0 = 4.473 - 5.933\text{i}$, $\omega_0 =$

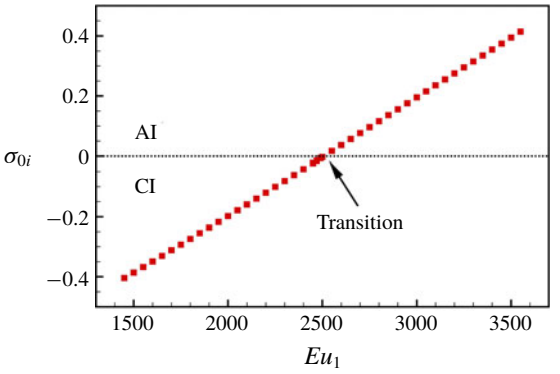

FIGURE 3. (Colour online) The absolute growth rate σ_{0i} versus Eu_1. $Re = 0.08$, $Eu_2 = 6.25 \times 10^6$, $M = 50$, $Du = 10^{-4}$.

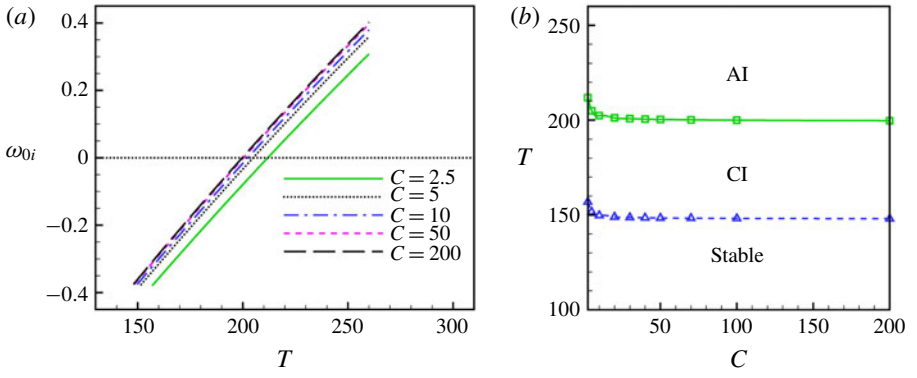

FIGURE 4. (Colour online) (*a*) The absolute growth rate ω_{0i} versus Taylor's parameter T for different values of the ion injection level C, and (*b*) the absolute and convective instability transition (the solid line with squares) and the temporally neutral stability boundary (the dashed line with triangles) in the C–T plane for transverse rolls. CI: convective instability; AI: absolute instability. The parameters in this figure are $M = 50$, $Fe = 10^4$.

$2.955 + 0.0128\mathrm{i}$). However, at a larger electric field $T = 1635$, the saddle point B becomes dominant with a larger ω_{0i} (this time, at A, $\alpha_0 = 0.991 - 1.515\mathrm{i}$, $\omega_0 = 1.628 + 0.0447\mathrm{i}$; at B, $\alpha_0 = 4.765 - 6.116\mathrm{i}$, $\omega_0 = 3.008 + 0.0695\mathrm{i}$). This saddle point shift makes a sudden turn of the lines in figure 5(*c*), which is indicated by an arrow there. In Delbende, Chomaz & Huerre (1998), a similar phenomenon was reported in their investigation of absolute/convective instabilities of the Batchelor vortex using direct numerical simulation. They observed a bump of absolute growth rate for the azimuthal mode -1 as the group velocity is increased. The saddle shift phenomenon in EHD-Poiseuille flow influences dramatically its dependence on M. In figure 5(*d*), one can see that the influence of the mobility ratio is great when its value is small, i.e. when the hydrodynamic mobility is not much larger than the ion mobility. At small M, the system remains convectively unstable unless T becomes extremely strong. A simple explanation of this result is that, in the momentum equation (2.15), the Coulomb force is proportional to M^2 and it being small indicates that, physically, the fluids are less

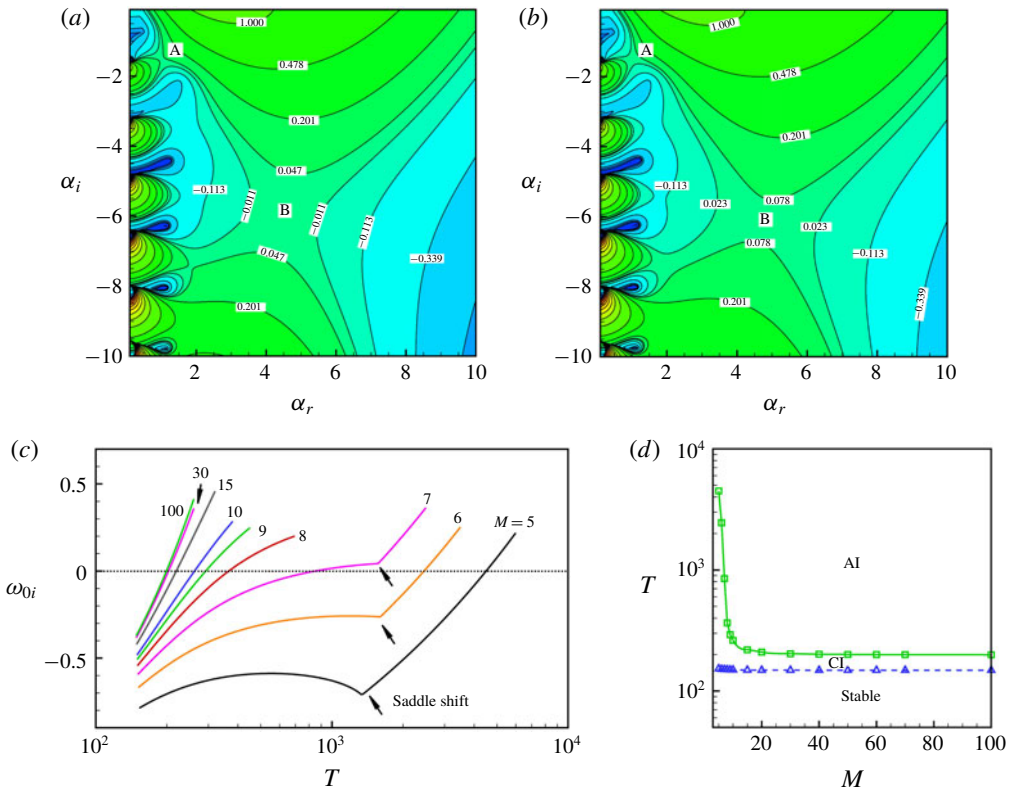

FIGURE 5. (Colour online) Contour of the absolute growth rate in the α plane featuring a saddle shift phenomenon at (*a*) $M = 7$, $T = 1495$ and (*b*) $M = 7$, $T = 1635$. (*c*) The absolute growth rate ω_{0i} versus Taylor's parameter T for different values of the mobility ratio M, and (*d*) the absolute and convective instability transition boundary (the solid line with squares) and the temporally neutral stability boundary (the dashed line with triangles) in the M–T plane for transverse rolls. The parameters in this figure are $C = 50$, $Fe = 10^4$.

affected by the electric field. As the Poiseuille flow is convectively unstable, small values of M will thus make EHD-Poiseuille flow more convectively unstable.

In order to further analyse the saddle point shift phenomenon, we plot the eigenfunctions at the two saddle points in figure 6 ($M = 6$, $T = 2453.229$) and figure 7 ($M = 7$, $T = 849.059$), respectively, at CI–AI transition. Interestingly, it can be seen in figure 6 that the eigenfunction of saddle point B is more localised in the vertical direction compared to that of saddle point A in figure 7. This implies that at smaller M when higher T is needed for absolute instability (saddle point B), the flow is more intensive in the vicinity of injecting plate ($y = 1$), a fact which might be interesting to experimentalists when they measure the intensity of the flow velocity. This will also stimulate theorists as spatially localised structures have been actively discussed in transition to turbulence (Eckhardt *et al.* 2007).

We summarise in the following the effect of M in the linear stability analysis of EHD-Poiseuille flow, which has been repeatedly discussed in the works by Castellanos & Agrait (1992), Lara *et al.* (1997), Zhang *et al.* (2015) with the new results of our calculation. For hydrostatic EHD flow (without a cross-flow $\mathcal{U} = 0$), the M effect can be deduced from (2.19), where we see that M^2 is a common factor for the

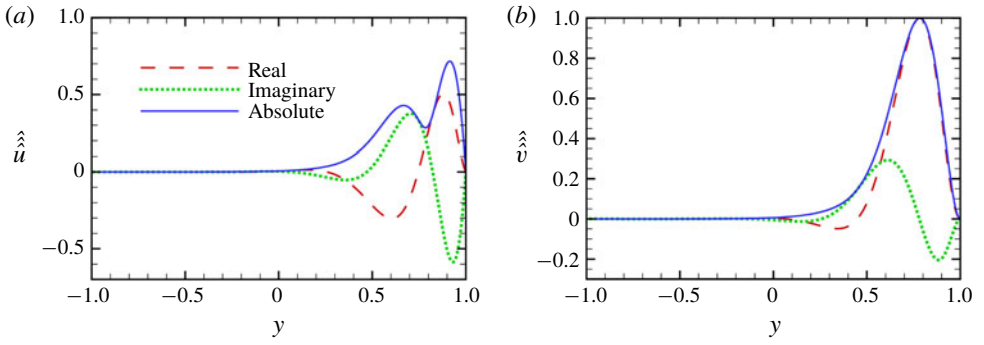

FIGURE 6. (Colour online) The eigenfunctions of (*a*) the streamwise velocity component u and (*b*) the normal velocity component v at $M = 6$ and $T = 2453.229$ (in this case saddle point B is dominant). $C = 50$, $Fe = 10^4$, $\mathcal{U} = 1$. The results are normalised by the maximum value of $\hat{\hat{v}}$.

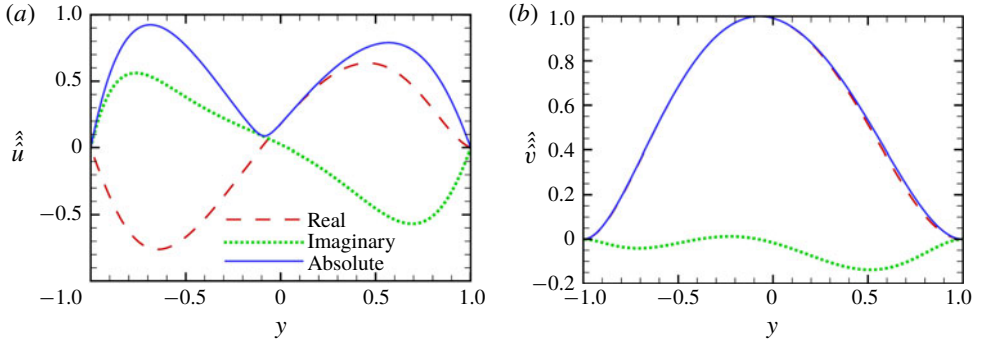

FIGURE 7. (Colour online) The eigenfunctions of (*a*) the streamwise velocity component u and (*b*) the normal velocity component v at $M = 7$ and $T = 849.059$ (in this case saddle point A is dominant). $C = 50$, $Fe = 10^4$, $\mathcal{U} = 1$. The results are normalised by the maximum value of $\hat{\hat{v}}$.

diffusion term and the terms related to the electric field. So, when the electric field is destabilising the flow, increasing M will lead to a more unstable flow; on the other hand, when the electric field stabilises the flow, increasing M will cause a more stable flow. Therefore, it can be said that increasing M promotes flow instability or stability. Especially, M has no effect on the neutral stability curve for the hydrostatic EHD flow. However, this does not hold true for $\mathcal{U} \neq 0$ in which case the terms involving $\mathcal{U}$ in (2.19) play an important role. Castellanos & Agrait (1992), Lara *et al.* (1997) reported a stabilising effect of M on the neutral stability curve in the limit of negligible charge diffusion effect ($Fe \to \infty$) and infinite charge injection ($C \to \infty$). We found that M has a very small influence on the stable–CI border, as shown in figure 5(*d*). This is related to our choice of $\mathcal{U} = 1$; in fact, at a larger value of $\mathcal{U}$, we do notice a remarkable effect of M on the stable–CI boundary, similar to Lara *et al.* (1997), see figure 9(*c*). On the other hand, M shows a significant influence on delimiting CI–AI transition, as shown in figure 5(*d*). From this figure, it is concluded

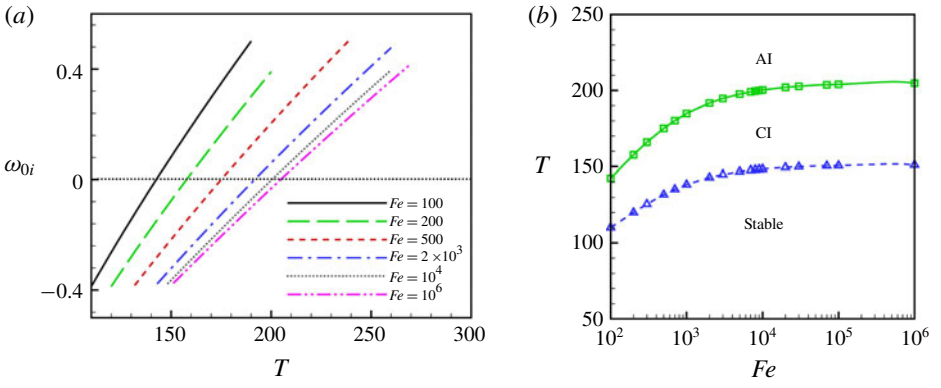

FIGURE 8. (Colour online) (*a*) The absolute growth rate ω_{0i} versus Taylor number T for different values of the reciprocal of the charge diffusion coefficient Fe, and (*b*) the absolute and convective instability transition boundary (the solid line with squares) and the temporally neutral stability boundary (the dashed line with triangles) in the Fe–T plane for transverse rolls. The parameters in this figure are $C = 50$, $M = 50$.

that increasing M at a constant T will lead the unstable flow to be more unstable (as it transits from being CI to AI), so on the CI–AI border, M has a destabilising effect. The rather steep slope at small M is related to the saddle point shift, as discussed for the first time for EHD-Poiseuille flow. It is interesting to note that at small M, when T increases, the more dominating saddle point will change from a point of smaller α_r to another point of larger α_r. At the same time, α_i becomes more negative. This shows that at small M, when T becomes larger, a shorter wave decaying faster in space is favoured in the transition from convective instability to absolute instability.

3.2.4. *Effect of Fe*

The charge diffusion effect, represented by the reciprocal of the dimensionless parameter Fe, also has some influence on the absolute and convective instabilities of the system. As shown in figure 8(*a*), as Fe decreases, the lines move towards the left, indicating that increasing the charge diffusion coefficient promotes the transition from convective to absolute instability of the system at a smaller T. In figure 8(*b*), the temporally stable domain is narrowed down as Fe decreases, meaning that increasing the charge diffusion effect may trigger the instability of the system at a weaker electric field, a finding similar to that by Zhang *et al.* (2015) for $\beta = 0$. Also, the critical T at which the transition from convective to absolute instability occurs increases as Fe increases, a result from which we can understand that the charge diffusion will facilitate absolute instability. In Zhang *et al.* (2015), the destabilising effect of charge diffusion on the stable–CI border is explained with the help of an energy analysis by calculating the energy transfer between the electric field and the hydrodynamic field. Since the trend of the CI–AI border is similar to that of the stable–CI border in figure 8(*b*), it may be hypothesised that a similar energy transfer between the two fields will also occur here. We believe that more work should be devoted to revealing the effect of charge diffusion. A more comprehensive study of the charge diffusion effect on flow stability/instability in EHD (and EHD-Poiseuille flow) is currently being undertaken by the authors.

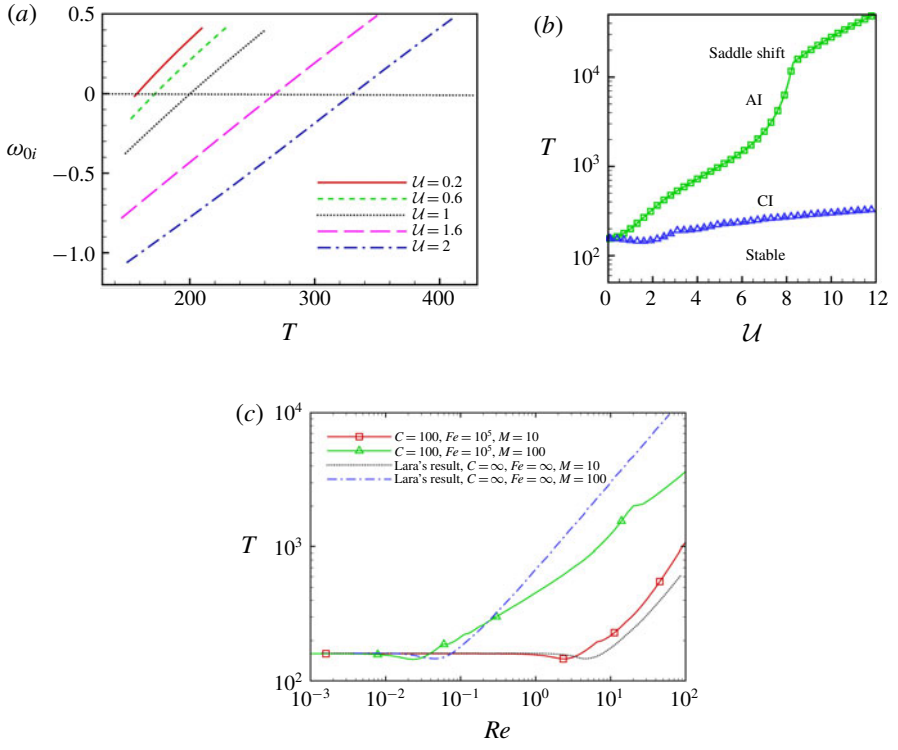

FIGURE 9. (Colour online) (*a*) The absolute growth rate ω_{0i} versus Taylor number T for different values of the base flow parameter $\mathcal{U}$, (*b*) the absolute and convective instability transition (the solid line with squares) and the temporally neutral stability boundary (the dashed line with triangles) in the $\mathcal{U}$–T plane for transverse rolls, and (*c*) comparison with the results in Lara *et al.* (1997). The parameters in (*a*,*b*) are $C = 50$, $M = 50$, $Fe = 10^4$.

3.2.5. *Effect of* $\mathcal{U}$

The parameter $\mathcal{U}$ represents the relative importance of the Poiseuille flow in the x direction. As shown in figure 9(*a*), the influence of $\mathcal{U}$ on the absolute and convective behaviours of the system is significant. In figure 9(*b*), there is also a shift of the saddle point on the CI–AI border. As $\mathcal{U}$ increases, the transition from convective to absolute instability can be greatly postponed, which reflects the convective instability nature of the Poiseuille flow (Deissler 1987). In contrast, as $\mathcal{U}$ decreases, the absolute instability can be triggered at a much weaker electric field, reflecting the absolute instability characteristics of electrohydrodynamic convection with no cross-flow. A similar figure to figure 9(*b*) can be found for RBP flow, for example, in the work by Müller *et al.* (1992). However, there is a noticeable difference that when $\mathcal{U}$ increases from 0, the critical T delimiting the stable–CI border decreases in the beginning and then increases. In RBP, the critical Ra as a function of Re increases monotonically ($\mathcal{U}$ is in proportion to Re), see Fujimura & Kelly (1988). Because of this and the fact that Ra_c for longitudinal rolls (LR, to be discussed below) is the same as that of RBC without a cross-flow, LR have a larger growth rate compared to TR. Experiments also confirmed that LR appear when Re is increases from 0. However, the situation is different in EHD-Poiseuille flow. As we have shown in figure 9(*b*), the critical T for

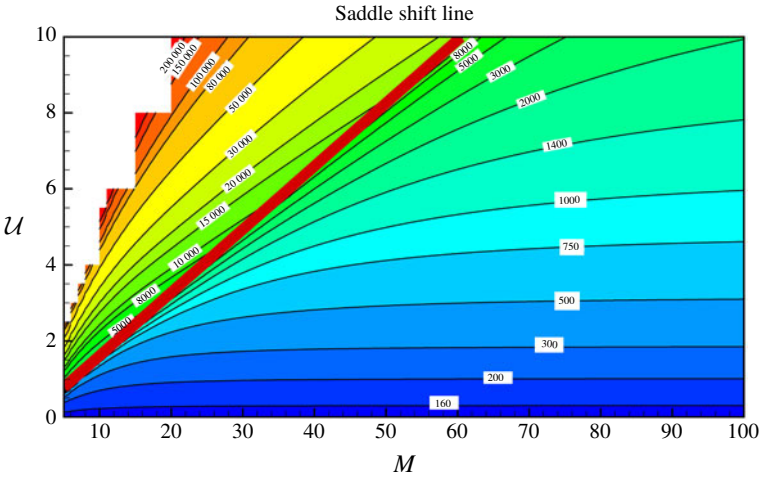

FIGURE 10. (Colour online) The contours of the Taylor number T at the border of absolute and convective instability in the M–$\mathcal{U}$ plane. $C = 50$, $Fe = 10^4$.

TR is smaller than that of LR (which is the same as the EHD without a cross-flow $\mathcal{U} = 0$) when $\mathcal{U}$ or Re is small, meaning that the growth rate of TR is larger than that of LR. Therefore, we deduce that TR will be a dominant pattern in EHD-Poiseuille when the amplitude of the cross-flow is small either because of convective instability or absolute instability. We also compare our results to those in Lara *et al.* (1997), shown in figure 9(*c*) regarding the stable–CI border. In their work, the injection level is infinite and the charge diffusion effect is neglected. We choose a large value of C approaching the SCL and a large value of Fe. The comparison is qualitatively satisfactory. The small dip at small Re discussed above also appears in all of the curves in this figure.

Finally, we combine the effects of $\mathcal{U}$ and M in a single plot depicting the critical T for the CI–AI transition, see figure 10 (we choose M because the effect of C is insignificant in SCL and the effect of Fe is less interesting than M). The previous results in figures 5(*d*) and 9(*b*) are simply two lines in this figure. At small values of M and large values of $\mathcal{U}$, the value of the critical T is so large that it is very difficult to calculate. The phenomenon of saddle point shift occurring at different values of M and $\mathcal{U}$ is also marked. This figure may serve as a guidance for experimentalists to do a preliminary parameter exploration in EHD-Poiseuille flow at the SCL condition.

We now discuss briefly the implication of our results on $\mathcal{U}$ and M for understanding the flow in ESP. The work by Atten *et al.* (1987) established the similarities between the flow properties of particles in air and ions in a liquid (having the same order of M value). Thus, to some extent, our results on ions in a liquid can be applied to the dynamics of the charged particles in the air flow of ESP, despite the facts that the geometries and the ion generation mechanisms in the flow problems are different and that the flow in ESP is turbulent, whereas we are conducting a spatio-temporal linear stability analysis. Leonard, Mitchner & Self (1983) conducted an experimental work on the EHD flow in ESP with the aim of minimising the generation of turbulence in ESP in order to improve its efficiency. Firstly, their finding that a smaller velocity in ESP led to an intensified turbulence level whereas a higher velocity abated turbulence level signals the convective effect

of the cross-flow which is consistent with our results shown in figure 9 (which implies that larger $\mathcal{U}$ will convect away the disturbance/turbulence). Secondly, the experimental results demonstrated that, for a smaller ion mobility ($\sim 1/M$ in our terminology), the disturbance/turbulence is less likely to be convected away (so the turbulence level increases), whereas, our result similarly indicates that larger M tends to result in an absolutely unstable flow, in which the disturbance/turbulence will be sustainable in a fixed frame of reference. Therefore, it is interesting to find that some of our results are consistent with the observations in Leonard *et al.* (1983) and we thus believe that the understanding of the dynamics of EHD flow in ESP may be improved by studying its absolute/convective instability. A more detailed work performing the linear AI/CI (or even nonlinear AI/CI in the spirit of Chomaz 1992) in the geometry of ESP would thus be very promising.

3.3. *Longitudinal rolls*

The absolute/convective instabilities of the longitudinal rolls ($\alpha = 0$) can be probed similarly to the transverse rolls. Because we are concerned with the absolute/convective instability of LR in the streamwise direction, the useful information in the complex α plane is restricted to only $\alpha = 0$ or $\alpha_r = 0$ (the former represents a constant amplitude longitudinal roll while the latter admits amplitude variation). We performed a numerical search of the saddle point simultaneously in the streamwise and transverse wavenumber spaces. Figure 11(*a*) shows the saddle point located at $\beta = 2.55$ in the β plane with a positive absolute growth rate for longitudinal rolls $\alpha = 0$ at $T = 200$, indicating that the flow is absolutely unstable in the transverse direction. This is a trivial result as there is no cross-flow in the transverse direction. The corresponding cusp point can be identified in the ω plane, as shown in (*b*), confirming its validity. When we look into the contour of ω_i in the α plane at $\beta = 2.55$ (*c*), there is no saddle point at $\alpha = 0$ (or $\alpha_r = 0$). In this case, the group velocity can be approximately calculated from (*d*) as 0.88 for $\mathcal{U} = 1$. Thus, these figures reveal no information about the growth rate at the ray $x/t = 0$ regarding absolute/convective instability of LRs. At the critical condition $T = 155.706$, we see the same behaviour of LR, as shown in figure 12. We also checked the other values of β for different T and a similar result is observed.

In order to gain some insight into the absolute/convective instabilities of longitudinal rolls, we present in the following a one-mode Galerkin approximation of (2.19) and (2.20) following Carrière & Monkewitz (1999). The trial mode for the vertical velocity is $a_1 v_1 = a_1(1-y^2)^2$ and for the electric potential $b_1\phi_1 = b_1(y^4 + 4y^3 - 18y^2 - 4y + 17)$, where a_1, b_1 are the coefficients. The slightly complex form of ϕ_1 is due to its boundary conditions (2.21*b*). Substituting these trial functions to the aforesaid equations, the one-mode Galerkin approximation leads to the following equations

$$\left(U\mathrm{i}\alpha(k^2 - D^2) + U''\mathrm{i}\alpha + \frac{M^2}{T}(k^4 - 2k^2D^2 + D^4)\right) a_1 v_1 + M^2[\Phi''' k^2 + \Phi' k^2(k^2 - D^2)] b_1\phi_1 - \mathrm{i}\omega(k^2 - D^2) a_1 v_1 = 0, \tag{3.1a}$$

$$-\Phi''' a_1 v_1 + \left[\Phi'''D + 2\Phi''(D^2 - k^2) + \Phi'(D^3 - k^2 D) + U\mathrm{i}\alpha(k^2 - D^2) + \frac{1}{Fe}(k^4 - 2k^2D^2 + D^4) - \mathrm{i}\omega(k^2 - D^2)\right] b_1\phi_1 = 0. \tag{3.1b}$$

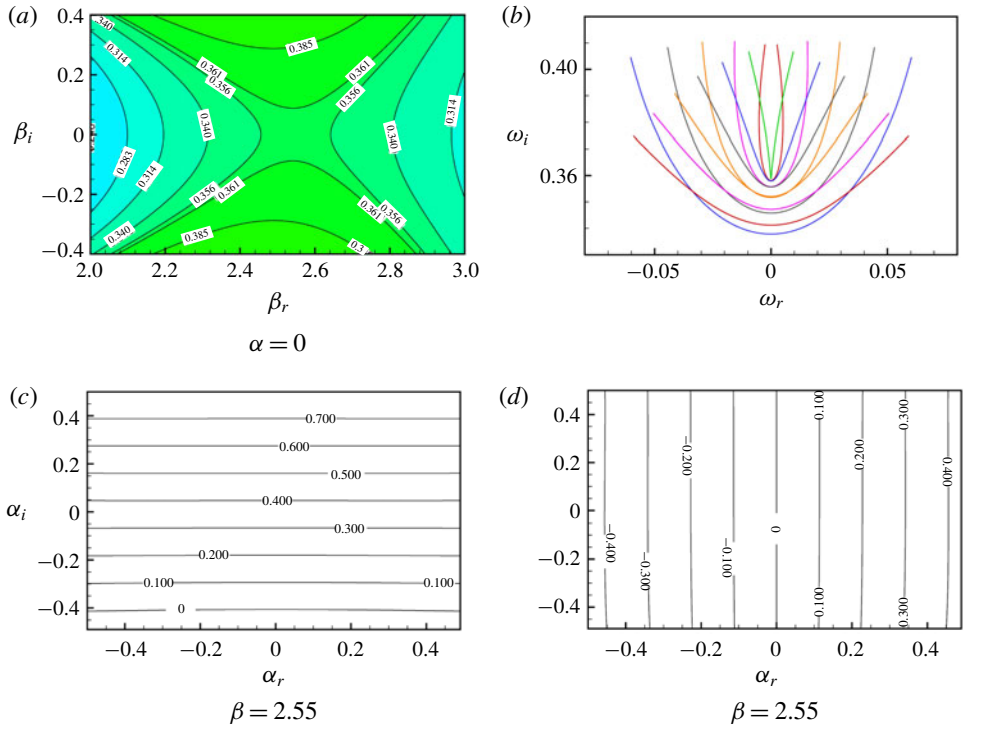

FIGURE 11. (Colour online) (*a*) Longitudinal rolls. (*b*) The cusp point in the ω plane. (*c*) Contour of ω_i when $\beta = 2.55$ in the α plane. There is no saddle point. (*d*) Contour of ω_r when $\beta = 2.55$ in the α plane $T = 200$, $C = 50$, $M = 50$, $Fe = 10^4$.

Multiplying the first equation with v_1, the second equation with ϕ_1 and integrating along the y direction, we have

$$\begin{pmatrix} \mathrm{i}\alpha f_1 + \dfrac{M^2}{T} f_2 - \mathrm{i}\omega f_3 & M^2 f_4 \\ -f_5 & f_6 + \mathrm{i}\alpha f_7 + \dfrac{1}{Fe} f_8 - \mathrm{i}\omega f_9 \end{pmatrix} \begin{pmatrix} a_1 \\ b_1 \end{pmatrix} = 0, \tag{3.2}$$

where $f_i > 0$ are some functions involving k^2. Applying the solvability condition, we have

$$\left(\alpha f_1 - \mathrm{i}\frac{M^2}{T} f_2 - \omega f_3\right)\left(-\mathrm{i}f_6 + \alpha f_7 - \mathrm{i}\frac{1}{Fe} f_8 - \omega f_9\right) - M^2 f_4 f_5 = 0. \tag{3.3}$$

Following Carrière & Monkewitz (1999), we substitute $\omega = \omega'' + \alpha(x/t)$ (ω'' is the temporal growth rate along the ray travelling at the group velocity x/t and $y/t = 0$) and take the derivative of the above equation with respect to α

$$\begin{aligned} &\left(f_1 - f_3 \frac{x}{t}\right)\left(-\mathrm{i}f_6 + \alpha f_7 - \mathrm{i}\frac{1}{Fe} f_8 - \omega'' f_9 - \alpha \frac{x}{t} f_9\right) \\ &\quad + \left(\alpha f_1 - \mathrm{i}\frac{M^2}{T} f_2 - \omega'' f_3 - \alpha \frac{x}{t} f_3\right)\left(f_7 - f_9 \frac{x}{t}\right) = 0. \end{aligned} \tag{3.4}$$

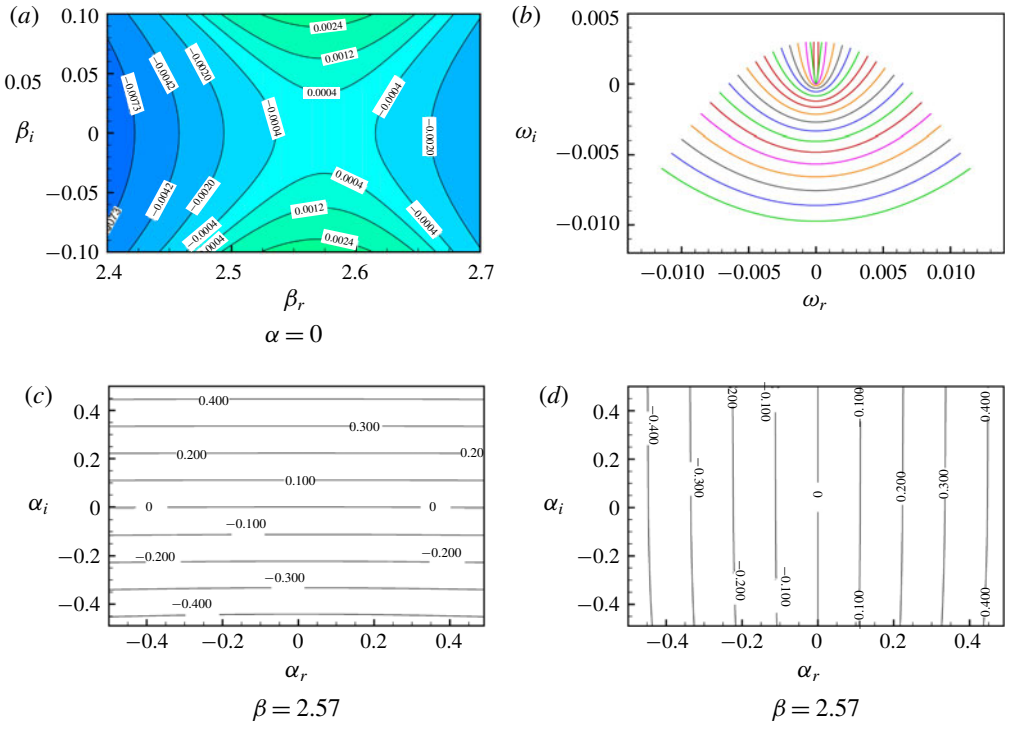

FIGURE 12. (Colour online) (*a*) Longitudinal rolls at the critical condition (to be consistent with the one-mode Galerkin approximation). (*b*) The cusp point in the ω plane. (*c*) Contour of ω_i when $\beta = 2.57$ in the α plane. There is no saddle point. (*d*) Contour of ω_r when $\beta = 2.57$ in the α plane $T = 155.706$, $C = 50$, $M = 50$, $Fe = 10^4$.

For longitudinal rolls $\alpha = 0$, a special case is considered as $\omega'' = 0$ at the criticality $T = T_c$ and $\beta = \beta_c$, so we have

$$\left(f_1 - f_3\frac{x}{t}\right)\left(f_6 + \frac{1}{Fe}f_8\right) + \frac{M^2}{T_c}f_2\left(f_7 - f_9\frac{x}{t}\right) = 0, \tag{3.5}$$

which is equivalent to

$$\left.\frac{x}{t}\right|_0 = \frac{f_1\left(f_6 + \dfrac{1}{Fe}f_8\right) + \dfrac{M^2}{T_c}f_2f_7}{f_3\left(f_6 + \dfrac{1}{Fe}f_8\right) + \dfrac{M^2}{T_c}f_2f_9}. \tag{3.6}$$

In order to investigate the growth rate in the vicinity of $x/t|_0$, we choose two rays $x/t_\pm$ on either side of $x/t|_0$ with $k^2 = 0$ and calculate the growth rates along these rays

$$0 < \frac{x}{t_-} = \frac{f_1}{f_3} = \frac{1}{3}\mathcal{U} < \left.\frac{x}{t}\right|_0, \quad \mathrm{Im}(\omega''_-) = -\frac{M^2}{T_c}\frac{f_2}{f_3} < 0, \tag{3.7a,b}$$

$$\frac{x}{t_+} = \frac{f_7}{f_9} = \frac{518}{153}\mathcal{U} > \left.\frac{x}{t}\right|_0, \quad \mathrm{Im}(\omega''_+) = -\frac{f_6 + \dfrac{1}{Fe}f_8}{f_9} < 0. \tag{3.7c,d}$$

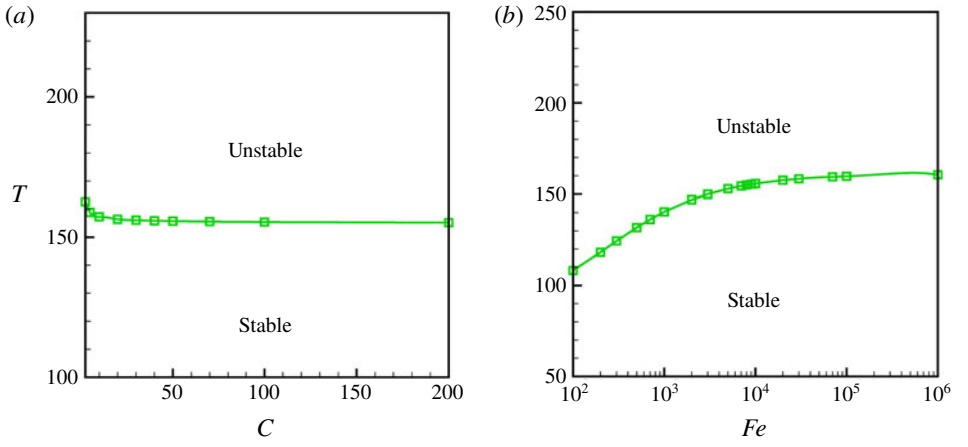

FIGURE 13. (Colour online) The neutral stability boundary in the C–T plane (a) and Fe–T plane (b) for longitudinal rolls. The parameters in this figure are $M = 50$, $Fe = 10^4$.

Note that the ray $x/t_- > 0$ is chosen to be the same as that in Carrière & Monkewitz (1999), while x/t_+ is different than theirs partially because of the different trial function used for the imposed electric field. As the base profile of the electric field depends on the values of C and Fe, we have checked many values of these two parameters and the results show that both the imaginary parts of ω'' are negative. It then can be deduced that at $x/t = 0$, the growth rate is negative, meaning that the flow cannot be absolutely unstable. Therefore, the LR is convectively unstable once there is a cross-flow.

With the convective nature of the longitudinal roll having been determined, we proceed to study the influence of the physical parameters on its instability. Figure 13 shows the neutral stability boundary in the C–T plane and the Fe–T plane. We see that the influence of the charge injection level C and charge diffusion coefficient Fe on the neutral stability boundary of longitudinal rolls is similar to their influence on transverse rolls as shown in figures 4(b) and 8(b), respectively.

The influence of the mobility ratio M on the temporal growth rate ω_i is shown in figure 14(a). In the stable region where $\omega_i < 0$, the stability of longitudinal rolls is reinforced by increasing the mobility ratio. However, in the unstable region where $\omega_i > 0$, the effect of the mobility ratio becomes destabilising. It is noted that the mobility ratio does not influence the critical value of T at which the transition from stability to instability occurs. The M effect in LR is the same as in static EHD without a cross-flow.

Finally, we consider the effect of the parameter $\mathcal{U}$. As shown in figure 14(b), the dependence of the temporal growth rate ω_i on T remains the same as $\mathcal{U}$ varies. That is, $\mathcal{U}$ has no influence on ω_i, which can be deduced as follows. When $\alpha = 0$, it can be seen in (2.19) and (2.20) that the U-related terms disappear because of their coupling to the streamwise spatial derivative. It is then the case that the magnitude of U will not influence the instability characteristics of longitudinal rolls. In RBP flow, a similar conclusion has been reached in the study of longitudinal rolls.

3.4. *Oblique rolls*

In the following, we show briefly the results for oblique rolls ($\alpha \neq 0$, $\beta \neq 0$). We first show in figure 15 that the growth rate of oblique rolls is always smaller than that of

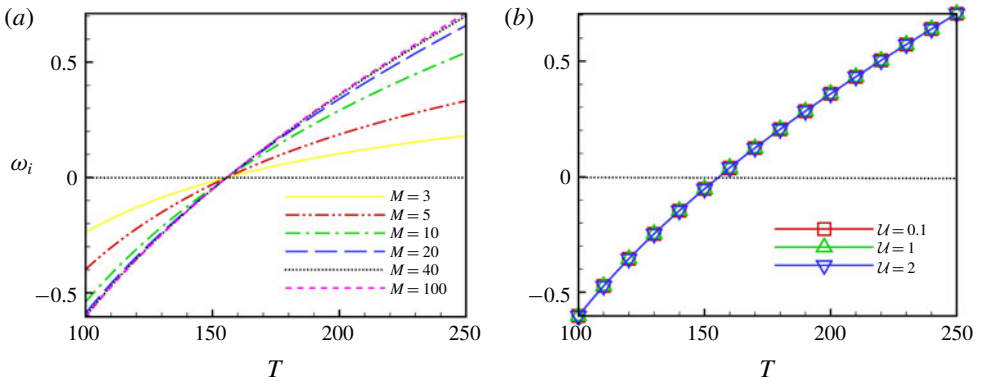

FIGURE 14. (Colour online) (*a*) The influence of the mobility ratio M on the growth rate ω_i of longitudinal rolls; (*b*) the influence of the base flow parameter $\mathcal{U}$. The parameters in this figure are $C = 50$, $M = 50$, $Fe = 10^4$.

TR or LR in temporal (left column in the figure) and spatial stability analyses (right column) as the maximum growth rate is found either on α or β axis. In RBP flow, it has also been demonstrated by Pearlstein (1985) that the most unstable mode should be either a transverse or a longitudinal roll.

To study the absolute and convective instability of oblique rolls, according to the method described in § 2.4, we need to find the saddle points in both the α and β planes, satisfying the pinching condition. Fortunately, due to the symmetry of the problem in the transverse direction, the maximum growth rate is found at $\beta = 0$. This is numerically examined in figure 16, in which we see that the absolute growth rate at the saddle point decreases when β increases. This indicates that the absolute growth rate for the transverse rolls is larger than that of oblique rolls. Such a numerical check only tackles one real line in the complex β plane. We also conducted a numerical search for the saddle points simultaneously in the complex α and β spaces and found that, in the β plane, the saddle point is always located at $\beta = 0$, confirming the transverse symmetry and implying that if the flow is absolutely unstable, TR will appear rather than an oblique roll. Therefore, we deduce that the oblique rolls are not significant in the CI–AI transition of EHD-Poiseuille flow and are not expected to be observed in the experiments. Oblique rolls were not present in the numerical simulations of RBP by Martinand, Carrière & Monkewitz (2006). In Carrière & Monkewitz (1999), they commented that the boundary of absolute instability in RBP coincides with the absolute instability boundary for transverse rolls due to transverse symmetry.

4. Concluding remarks

In this work, we have applied spatio-temporal linear stability analysis to EHD-Poiseuille flow in the SCL regime in order to investigate its absolute and convective instabilities, supplementing the previous studies on the linear stability analysis of this flow (Castellanos & Agrait 1992; Lara *et al.* 1997; Zhang *et al.* 2015). We considered three different roll structures. Physical parameters such as T, M, C, Fe, $\mathcal{U}$ are probed with an aim of clarifying their effects on the absolute–convective instability transition. These results are important to understand in general the effect of an electric field

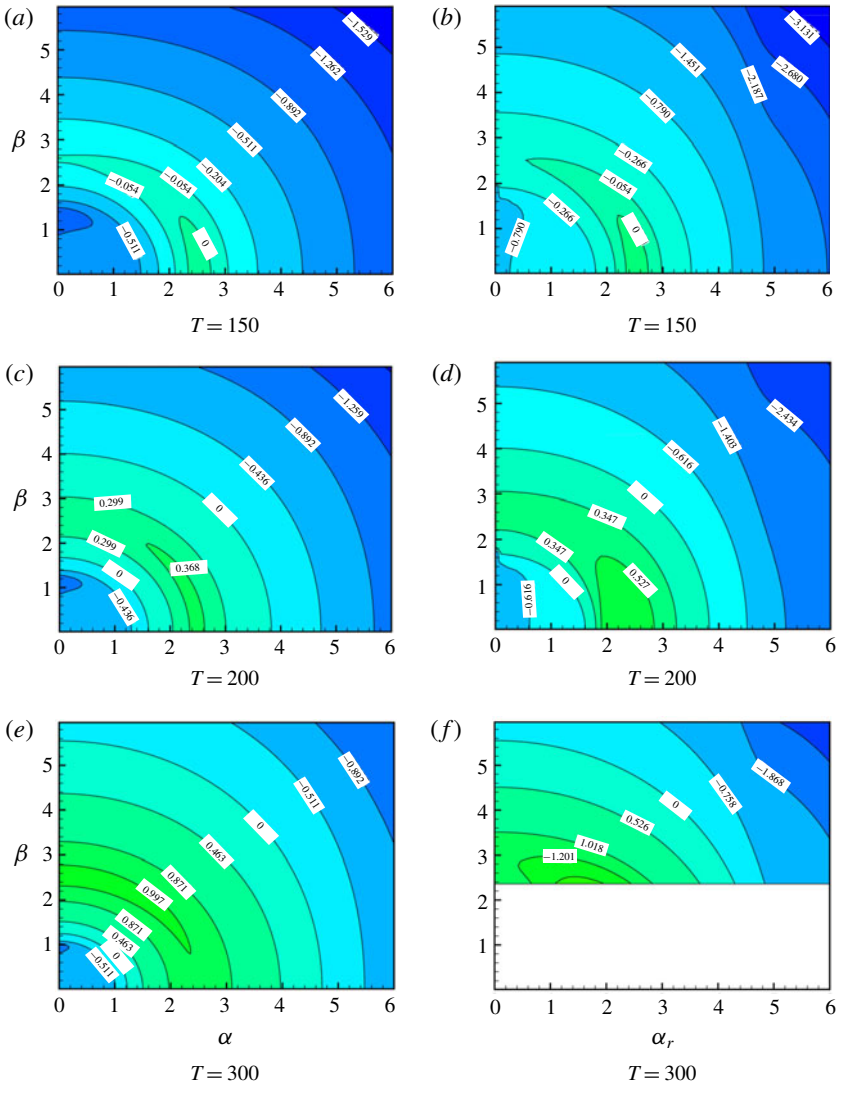

FIGURE 15. (Colour online) (*a*,*c*,*e*) Typical ω_i-contours in the α–β plane for the temporal instability of oblique rolls; (*b*,*d*,*f*) typical $-\alpha_i$-contours in the α_r–β plane for the spatial instability of oblique rolls. The parameters in this figure are $C = 50$, $M = 50$, $Fe = 10^4$. Note that in (*f*) in the region where the transverse number β is smaller than 2.34 the rolls become absolutely unstable and spatial analysis cannot be used.

applied in a cross-flow, for example, in the case of electrostatic precipitators, flow control or heat transfer enhancement using EHD.

The effects of non-dimensional parameters are briefly summarised here. For TR, we found that increasing T (Coulomb force to viscous force) or electric voltage V_0 will make the flow transition from being convectively unstable to absolutely unstable. Since the flow we considered is in the SCL regime, the effect of the ion injection level C on the CI–AI transition is not significant except at small C. Small mobility ratio M is associated with a saddle point shift phenomenon and subsequently, the

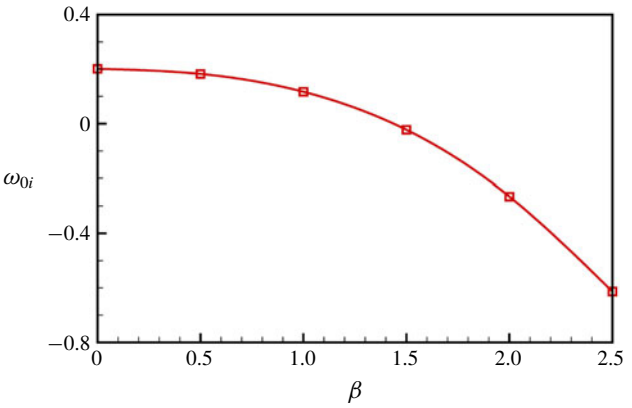

FIGURE 16. (Colour online) The absolute growth rate ω_{0i} as a function of β at saddle points (each data point corresponds to a saddle point). This figure aims to show at $\beta = 0$, the absolute growth rate is maximum. $T = 230$, $\mathcal{U} = 1$, $C = 50$, $M = 50$, $Fe = 10^4$. $\beta = 0$ represents transverse rolls and $\beta \neq 0$ oblique rolls.

critical T in this condition for CI–AI transition is boosted to a much higher value. Physically this is because that small M tends to make the hydrodynamical field decouple from the electric effect, rendering it more stringent to becoming absolutely unstable (due to the convective nature of Poiseuille flow). Stronger charge diffusion will facilitate flow instability, towards absolute instability. Understanding its instability mechanism is beyond the current work and is currently under investigation. The critical T increases with increasing magnitude of the cross-flow.

This paper is written with an objective to serve as a source of comparison and theoretical guidance for future laboratory measurements of the absolute/convective instabilities in a real dielectric fluid subject to unipolar injection. Our findings that the experimentalists may find useful and interesting and are subject to verification include that (i) near CI–AI transition, the absolute growth rate increases quadratically as a function of the applied voltage (which is the most straightforward means to change in experiments), that (ii) when T is large and M relatively small, localised flow structures appear close to the injector at the saddle condition and that (iii) when the amplitude of the cross-flow is small, TR is more likely to appear in the experiments than LR and the TR can exhibit absolute instability in EHD-Poiseuille flow. When $\mathcal{U}$ is large, LR has a higher growth rate than TR and is preferred at this condition. Besides, our results also show that the LR is convectively unstable and for oblique rolls, the growth rate is always smaller than that of TR/LR.

This work focuses on the linear nature of the absolute and convective instabilities in EHD-Poiseuille flow. When the disturbance grows to some extent, a nonlinear analysis is employed for the subsequent development of the disturbance, for which a direct numerical method is usually employed. A nonlinear analysis (Chomaz 1992) is suggested to be undertaken in the future as it will reveal more thoroughly the roll transition mechanism in EHD-Poiseuille flow. Besides, the absolute/convective instability in other EHD flows subject to a cross-flow, which are more directly related to the practical problems, such as wire-two-plate geometry in McCluskey & Atten (1984) and ESP (Leonard *et al.* 1983; Atten *et al.* 1987), can be studied similarly, as we have suggested above.

Acknowledgements

F.L. and B.W. acknowledge the financial support by the National Natural Science Foundation of China (Project nos. 11772328, 11621202 and 11502137). M.Z. acknowledges the Start-up grant from the Ministry of Education, Singapore (MOE WBS no. R-265-000-619-133). We thank all the referees for their constructive suggestions.

Appendix A. Method to find saddle points

A double iteration method is used to calculate saddle points in the three-dimensional case. The procedure is as follows: first, give four initial values of β, i.e. β_1, β_2, β_3 and β_4, near a saddle point in the complex β-plane; for each initial value of β, i.e. β_j, calculate the corresponding saddle point in the complex α-plane using the iteration method employed in Yin & Sun (2003). That is, given four values of α, i.e. α_1, α_2, α_3 and α_4, near the saddle point, calculate the corresponding values of ω, i.e. ω_1, ω_2, ω_3 and ω_4, and then construct the following interpolation function

$$\omega(\alpha_i) = \frac{a}{3}(\alpha_i - \alpha_4)^3 + \frac{b}{2}(\alpha_i - \alpha_4)^2 + c(\alpha_i - \alpha_4) + d, \tag{A 1}$$

where the subscript $i = 1, 2, 3, 4$. The coefficients a, b, c and d are readily solved by substituting the four couples of α and ω into (A 1). Naturally, the value of α at the saddle point is supposed to be the solution of the following equation

$$\frac{\mathrm{d}\omega}{\mathrm{d}\alpha} = a(\alpha - \alpha_4)^2 + b(\alpha - \alpha_4) + c = 0. \tag{A 2}$$

Solving (A 2), we obtain α_5. Then we use α_2, α_3, α_4 and α_5 as four known values in the interpolation function (A 1), and calculate the saddle point again in (A 2). The iteration is terminated when a convergence request is reached (e.g. the relative error of α or ω is not larger than 0.005). Thus we obtain α_{0j} and ω_{0j} at the saddle point in the complex α-plane that correspond to β_j; then, in complex β-plane, four couples of β_j and ω_{0j} are used to build an interpolation function similar to (A 1)

$$\omega(\beta_j) = \frac{a}{3}(\beta_j - \beta_4)^3 + \frac{b}{2}(\beta_j - \beta_4)^2 + c(\beta_j - \beta_4) + d, \tag{A 3}$$

where $j = 1, 2, 3, 4$, and the saddle point in the complex β-plane is determined by

$$\frac{\mathrm{d}\omega}{\mathrm{d}\beta} = a(\beta - \beta_4)^2 + b(\beta - \beta_4) + c = 0. \tag{A 4}$$

Solving (A 4), we obtain β_5; for this β_5, Yin & Sun's iteration method is used again to calculate the corresponding α_{05} and ω_{05} at the saddle point in the complex α-plane; then, replacing β_1, ω_{01} by β_5, ω_{05} in (A 3), we calculate β_6 ... until it converges. Finally we get the values of α_0, β_0 and ω_0 at the saddle points in both the complex α- and complex β-planes. For an overview of the numerical methods of locating saddle points in wavenumber space using the viscous dispersion relation, one is referred to Suslov (2006).

REFERENCES

ALLEN, P. H. G. & KARAYIANNIS, T. G. 1995 Electrohydrodynamic enhancement of heat transfer and fluid flows. *Heat Recovery Systems CHP* **15** (5), 389–423.

ATTEN, P., CAPUTO, J. G., MALRAISON, B. & GAGNE, Y. 1984 Détermination de dimension d'attracteurs pour differents écoulements. *J. Méc. Theor. Appl.* 133–156 (numéro spécial).

ATTEN, P. & HONDA, T. 1982 The electroviscous effect and its explanation I-The electrohydrodynamic origin; study under unipolar D.C. injection. *J. Electrostat.* **11** (3), 225–245.

ATTEN, P. & LACROIX, J. C. 1974 Stabilité hydrodynamique non-linéaire d'un liquide isolant soumis à une injection unipolaire forte. *C. R. Acad. Sci. Paris T.278,* B 385–387.

ATTEN, P. & LACROIX, J. C. 1979 Non-linear hydrodynamic stability of liquids subjected to unipolar injection. *J. Méc.* **18**, 469–510.

ATTEN, P., MCCLUSKEY, F. M. J. & LAHJOMRI, A. C. 1987 The electrohydrodynamic origin of turbulence in electrostatic precipitators. *IEEE Trans. Ind. Applics.* **IA-23** (4), 705–711.

ATTEN, P. & MOREAU, R. 1972 Stabilité electrohydrodynamique des liquides isolants soumis à une injection unipolaire. *J. Méc.* **11**, 471–520.

BERS, A. 1983 Space-time evolution of plasma instabilities-absolute and convective. In *Handbook of Plasma Physics* (ed. M. N. Rosenbluth & R. Z. Sagdeev), vol. 1, pp. 451–517. North-Holland.

BRIGGS, R. J. 1964 *Electron-Stream Interaction with Plasmas*. Massachusetts.

CARRIÈRE, P. & MONKEWITZ, P. A. 1999 Convective versus absolute instability in mixed Rayleigh–Bénard–Poiseuille convection. *J. Fluid Mech.* **384**, 243–262.

CARRIÈRE, P., MONKEWITZ, P. A. & MARTINAND, D. 2004 Envelope equations for the Rayleigh–Bénard–Poiseuille system. Part 1. Spatially homogeneous case. *J. Fluid Mech.* **502**, 153–174.

CASTELLANOS, A. 1991 Coulomb-driven convection in electrohydrodynamics. *IEEE Trans. Elec. Insul.* **26** (6), 1201–1215.

CASTELLANOS, A. 1998 *Electrohydrodynamics*. Springer.

CASTELLANOS, A. & AGRAIT, N. 1992 Unipolar injection induced instabilities in plane parallel flows. *IEEE Trans. Ind. Applics.* **28** (3), 513–519.

CHAKRABORTY, S., LIAO, I.-C., ADLER, A. & LEONG, K. W. 2009 Electrohydrodynamics: a facile technique to fabricate drug delivery systems. *Adv. Drug Deliv. Rev.* **61** (12), 1043–1054.

CHEN, C.-H., LIN, H., LELE, S. K. & SANTIAGO, J. G. 2005 Convective and absolute electrokinetic instability with conductivity gradients. *J. Fluid Mech.* **524**, 263–303.

CHOMAZ, J. M. 1992 Absolute and convective instabilities in nonlinear systems. *Phys. Rev. Lett.* **69**, 1931–1934.

CHOMAZ, J.-M. 2005 Global instabilities in spatially developing flows: non-normality and nonlinearity. *Annu. Rev. Fluid Mech.* **37**, 357–392.

CROSS, M. C. 1980 Derivation of the amplitude equation at the Rayleigh–Bénard instability. *Phys. Fluids* **23** (9), 1727–1731.

DARABI, J., RADA, M., OHADI, M. & LAWLER, J. 2002 Design, fabrication, and testing of an electrohydrodynamic ion-drag micropump. *J. Microelectromech. Syst.* **11** (6), 684–690.

DEISSLER, R. J. 1987 The convective nature of instability in plane Poiseuille flow. *Phys. Fluids* **30** (8), 2303–2305.

DELBENDE, I., CHOMAZ, J.-M. & HUERRE, P. 1998 Absolute/convective instabilities in the Batchelor vortex: a numerical study of the linear impulse response. *J. Fluid Mech.* **355**, 229–254.

DUBOIS, M. 1982 Experimental aspects of the transition to turbulence in Rayleigh–Bénard convection. In *Stability of Thermodynamics Systems* (ed. J. Casas-Vázquez & G. Lebon), pp. 177–191. Springer.

ECKHARDT, B., SCHNEIDER, T. M., HOF, B. & WESTERWEEL, J. 2007 Turbulence transition in pipe flow. *Annu. Rev. Fluid Mech.* **39** (1), 447–468.

FÉLICI, N. 1971 DC conduction in liquid dielectrics. Part II: electrohydrodynamic phenomena. *Direct Current Power Electron.* **2**, 147–165.

FRISCH, U. & MORF, R. 1981 Intermittency in nonlinear dynamics and singularities at complex times. *Phys. Rev.* A **23**, 2673–2705.

FUJIMURA, K. & KELLY, R. E. 1988 Stability of unstably stratified shear flow between parallel plates. *Fluid Dyn. Res.* **2** (4), 281–292.

FUJIMURA, K. & KELLY, R. E. 1995 Interaction between longitudinal convection rolls and transverse waves in unstably stratified plane Poiseuille flow. *Phys. Fluids* **7** (1), 68–79.

GAGE, K. S. & REID, W. H. 1968 The stability of thermally stratified plane Poiseuille flow. *J. Fluid Mech.* **33** (01), 21–32.

GASTER, M. 1965 On the generation of spatially growing waves in a boundary layer. *J. Fluid Mech.* **22** (03), 433–441.

GASTER, M. 1968 Growth of disturbances in both space and time. *Phys. Fluids* **11** (4), 723–727.
GASTER, M. 1975 A theoretical model of a wave packet in the boundary layer on a flat plate. *Proc. R. Soc. Lond.* A **347** (1649), 271–289.
GASTER, M. 1981 Propagation of linear wave packets in laminar boundary layers. *AIAA J.* **19** (4), 419–423.
GRANDJEAN, E. & MONKEWITZ, P. A. 2009 Experimental investigation into localized instabilities of mixed Rayleigh–Bénard–Poiseuille convection. *J. Fluid Mech.* **640**, 401–419.
HUERRE, P. & MONKEWITZ, P. A. 1985 Absolute and convective instabilities in free shear layers. *J. Fluid Mech.* **159**, 151–168.
HUERRE, P. & MONKEWITZ, P. A. 1990 Local and global instabilities in spatially developing flows. *Annu. Rev. Fluid Mech.* **22**, 473–537.
KELLY, R. E. 1994 The onset and development of thermal convection in fully developed shear flows. *Adv. Appl. Mech.* **31**, 35–112.
KIKUCHI, H. 2001 *Electrohydrodynamics in Dusty and Dirty Plasmas*. Kluwer Academic Publishers.
KOURMATZIS, A. & SHRIMPTON, J. S. 2014 Electrohydrodynamic inter-electrode flow and liquid jet characteristics in charge injection atomizers. *Exp. Fluids* **55** (3), 1688.
KOURMATZIS, A. & SHRIMPTON, J. S. 2016 Characteristics of electrohydrodynamic roll structures in laminar planar Couette flow. *J. Phys.* D*: Appl. Phys.* **49** (4), 045503.
KUPFER, K., BERS, A. & RAM, A. K. 1987 The cusp map in the complex-frequency plane for absolute instabilities. *Phys. Fluids* **30** (10), 3075–3082.
LACROIX, J. C., ATTEN, P. & HOPFINGER, E. J. 1975 Electro-convection in a dielectric liquid layer subjected to unipolar injection. *J. Fluid Mech.* **69** (03), 539–563.
LARA, J. L., CASTELLANOS, A. & PONTIGA, F. 1997 Destabilization of plane Poiseuille flow of insulating liquids by unipolar charge injection. *Phys. Fluids* **9** (2), 399–406.
LEONARD, G. L., MITCHNER, M. & SELF, S. A. 1983 An experimental study of the electrohydrodynamic flow in electrostatic precipitators. *J. Fluid Mech.* **127**, 123–140.
MALRAISON, B. & ATTEN, P. 1982 Chaotic behavior of instability due to unipolar ion injection in a dielectric liquid. *Phys. Rev. Lett.* **49** (10), 723–726.
MARTINAND, D., CARRIÈRE, P. & MONKEWITZ, P. A. 2006 Three-dimensional global instability modes associated with a localized hot spot in Rayleigh–Bénard–Poiseuille convection. *J. Fluid Mech.* **551**, 275–301.
MCCLUSKEY, F. M. J. & ATTEN, P. 1984 Entrainment of an injected unipolar space charge by a forced flow in a rectangular channel. *J. Electrostat.* **15** (3), 329–342.
MELCHER, J. R. & FIREBAUGH, M. S. 1967 Traveling-wave bulk electroconvection induced across a temperature gradient. *Phys. Fluids* **10** (6), 1178–1185.
MÜLLER, H. W., LÜCKE, M. & KAMPS, M. 1992 Transversal convection patterns in horizontal shear flow. *Phys. Rev.* A **45** (6), 3714–3726.
MÜLLER, H. W., TVEITEREID, M. & TRAINOFF, S. 1993 Rayleigh–Bénard problem with imposed weak through-flow: two coupled Ginzburg–Landau equations. *Phys. Rev.* E **48**, 263–272.
PARDON, G., LADHANI, L., SANDSTRÖM, N., ETTORI, M., LOBOV, G. & VAN DER WIJNGAART, W. 2015 Aerosol sampling using an electrostatic precipitator integrated with a microfluidic interface. *Sensors Actuators* B **212**, 344–352.
PEARLSTEIN, A. J. 1985 On the two-dimensionality of the critical disturbances for stratified viscous plane parallel shear flows. *Phys. Fluids* **28** (2), 751–753.
PÉREZ, A. T. & CASTELLANOS, A. 1989 Role of charge diffusion in finite-amplitude electroconvection. *Phys. Rev.* A **40** (10), 5844–5855.
RICHARDSON, A. T. & DEO, B. J. S. 1986 Nonlinear stability bounds for plane Poiseuille flow subjected to unipolar charge injection. *Q. J. Mech. Appl. Maths* **39** (1), 25–40.
SAVILLE, D. A. 1997 Electrohydrodynamics: the Taylor–Melcher leaky dielectric model. *Annu. Rev. Fluid Mech.* **29** (1), 27–64.
SCHMID, P. J. 2007 Nonmodal stability theory. *Annu. Rev. Fluid Mech.* **39**, 129–162.
SCHOPPA, W. & HUSSAIN, F. 1998 A large-scale control strategy for drag reduction in turbulent boundary layers. *Phys. Fluids* **10** (5), 1049–1051.
SHRIMPTON, J. S. 2009 *Charge Injection Systems: Physical Principles, Experimental and Theoretical Work*. Springer.

STUETZER, O. M. 1960 Ion drag pumps. *J. Appl. Phys.* **31** (1), 136–146.

SUSLOV, S. A. 2006 Numerical aspects of searching convective/absolute instability transition. *J. Comput. Phys.* **212** (1), 188–217.

TVEITEREID, M. & MÜLLER, H. W. 1994 Pattern selection at the onset of Rayleigh–Bénard convection in a horizontal shear flow. *Phys. Rev.* E **50**, 1219–1226.

WHITE, H. J. 1965 *Industrial Electrostatic Precipitation*. Addison-Wesley.

WHITHAM, G. B. 1974 *Linear and Nonlinear Waves*. Wiley.

YIN, X. & SUN, D. 2003 *Vortex Stability*. National Defense Industry Press.

ZHANG, M. 2016 Weakly nonlinear stability analysis of subcritical electrohydrodynamic flow subject to strong unipolar injection. *J. Fluid Mech.* **792**, 328–363.

ZHANG, M., MARTINELLI, F., WU, J., SCHMID, P. J. & QUADRIO, M. 2015 Modal and nonmodal stability analysis of electrohydrodynamic flow with and without cross-flow. *J. Fluid Mech.* **770**, 319–349.